



HAL
open science

The April 2010 North African heatwave: when the water vapor greenhouse effect drives nighttime temperatures

Yann Llargeron, Françoise Guichard, Romain Roehrig, Fleur Couvreur, Jessica Barbier

► To cite this version:

Yann Llargeron, Françoise Guichard, Romain Roehrig, Fleur Couvreur, Jessica Barbier. The April 2010 North African heatwave: when the water vapor greenhouse effect drives nighttime temperatures. *Climate Dynamics*, 2020, 54 (9-10), pp.3879-3905. 10.1007/s00382-020-05204-7 . hal-04816378

HAL Id: hal-04816378

<https://cnrs.hal.science/hal-04816378v1>

Submitted on 26 Jan 2025

HAL is a multi-disciplinary open access archive for the deposit and dissemination of scientific research documents, whether they are published or not. The documents may come from teaching and research institutions in France or abroad, or from public or private research centers.

L'archive ouverte pluridisciplinaire **HAL**, est destinée au dépôt et à la diffusion de documents scientifiques de niveau recherche, publiés ou non, émanant des établissements d'enseignement et de recherche français ou étrangers, des laboratoires publics ou privés.



Distributed under a Creative Commons Attribution 4.0 International License

Noname manuscript No.
(will be inserted by the editor)

1 **The April 2010 North African heatwave: when the water vapor**
2 **greenhouse effect drives nighttime temperatures**

3 **Yann Largeron · Françoise Guichard · Romain**
4 **Roehrig · Fleur Couvreur · Jessica Barbier**

5
6 Received: date / Accepted: date

7 **Abstract** North Africa experienced a severe heatwave in April 2010 with daily maximum
8 temperatures (T_{max}) frequently exceeding $40^{\circ}C$ and daily minimum temperatures (T_{min}) over
9 $27^{\circ}C$ for more than five consecutive days in extended Saharan and Sahelian areas. Obser-
10 vations show that areas and periods affected by the heatwave correspond to strong positive
11 anomalies of surface incoming longwave fluxes (LW_{in}) and negative anomalies of incoming
12 shortwave fluxes (SW_{in}). The latter are explained by clouds in the Sahara, and by both clouds
13 and dust loadings in the Sahel. However, the strong positive anomalies of LW_{in} are hardly
14 related to cloud or aerosol radiative effects.

15 An analysis based on climate-model simulations (CNRM-AM) complemented by a
16 specially-designed conceptual soil-atmospheric surface layer model (SARAWI) shows that
17 this positive anomaly of LW_{in} is mainly due to a water vapor greenhouse effect. SARAWI,
18 which represents the two processes driving temperatures, namely turbulence and longwave
19 radiative transfer between the soil and the atmospheric surface layer, points to the crucial
20 impact of synoptic low-level advection of water vapor on T_{min} . By increasing the atmo-
21 spheric infrared emissivity, the advected water vapor dramatically increases the nocturnal
22 radiative warming of the soil surface, then in turn reducing the nocturnal cooling of the at-
23 mospheric surface layer, which remains warm throughout the night. Over Western Sahel,
24 this advection is related to an early northward incursion of the monsoon flow. Over Sahara,
25 the anomalously high precipitable water is due to a tropical plume event. Both observations
26 and simulations support this major influence of the low-level water vapor radiative effect on
27 T_{min} during this spring heatwave.

28 **Keywords** Heatwave · Radiative physics · Greenhouse effect · North Africa

Y. Largeron
CNRS-CNRM/GMME/MOANA
E-mail: yann.largeron@meteo.fr, ylargeron@gmail.com
Tel : +33 561079312

29 1 Introduction

30 Heatwaves and their impacts over Europe or Western countries have been widely studied
31 (e.g. [Beniston, 2004], [Black et al., 2004], [Perkins, 2015] for a review). They received
32 much less attention elsewhere, especially in North Africa. However, climate projections
33 indicate that North Africa, where climate is among the warmest and driest on Earth, will
34 be particularly affected by climate changes in a near future [Roehrig et al., 2013; Deme
35 et al., 2017]. Furthermore, heatwaves have become more frequent and severe in the past
36 three decades [Fontaine et al., 2013; Moron et al., 2016] and these trends are projected to
37 continue [IPCC, 2013]. This could become an exacerbating factor of vulnerability of North
38 African societies whose adaptation strategies appear limited, due to their low hydrological
39 resources and agricultural productivity [IPCC, 2014; Sultan and Gaetani, 2016].

40 In the Sahel, springtime has exhibited a strong trend of climate warming since 1950
41 [Guichard et al., 2012, 2017], up to twice the corresponding trend observed over Europe.
42 This strong warming more significantly occurs during the hottest months of the year (April,
43 May), at the end of the dry season, before the onset of the West African monsoon. This
44 combination leads to heatwaves of unprecedented strong magnitude, an example of which
45 occurred in spring 2010, where temperature peaks higher than 45°C were recorded in many
46 Sahelian countries (Niger, Senegal, Mali, Burkina Faso and Chad). These very high temper-
47 atures had strong impacts on morbidity and mortality (e.g. [Honda et al., 2014]).

48 Progressive multi-day soil desiccation has been recently pointed out as a major process
49 operating during mid-latitude mega-heatwaves, like those who took place in Europe in 2003
50 or in Russia in 2010 ([Miralles et al., 2014; Fischer, 2014]). However, this process is unlikely
51 to operate over North Africa during springtime since soils are mostly dry at this period of
52 the year and remain so until the arrival of the monsoon rain (e.g. [Baup et al., 2007]). In
53 contrast, Sahelian heatwaves appear to be frequently associated with an increase of moisture
54 ([Guichard et al., 2009] and further evidences in the present study). Physical mechanisms
55 operating during these heatwaves therefore still need to be identified.

56 Using in-situ observations in the central Sahel, Guichard et al. [2009] show that night-
57 time minimum temperatures increase by several degrees during the first incursions of the
58 moist monsoon flow in spring, while the incoming longwave flux at the surface varies ac-
59 cordingly. Therefore, couplings between surface air temperature, humidity and radiative
60 fluxes are expected, particularly during nighttime. On the other hand, springtime in the Sahel
61 is often associated with high dust loadings [Brooks and Legrand, 2000; Basart et al., 2009;
62 Klose et al., 2010], mid-level clouds and cirrus. These processes are likely to limit daytime
63 incoming fluxes, boundary layer growth and therefore daytime warming. These contrasting
64 impacts on low-levels suggest a strong diurnal cycle of the physical processes acting during
65 springtime heatwaves, implying reduced daytime warming and reduced nighttime cooling
66 with partly compensating effects on daily-average temperatures in unknown proportions.

67 Over the Sahel and Sahara, the surface and Top Of Atmosphere (TOA) energy budget
68 is affected by aerosols, that are known to have a radiative impact both in the longwave and
69 shortwave band, generally leading to a negative net effect [Balkanski et al., 2007]. Similarly,
70 cloud cover induce a longwave warming generally overcompensated by a shortwave cooling
71 [Bouniol et al., 2012]. Recently, Marsham et al. [2016] studied the respective impacts of
72 water vapor and dust aerosols in controlling the radiative budget over the Sahara, using
73 both in-situ observations and satellite retrievals. They concluded that the total column water
74 vapor provides a stronger control on TOA net radiative fluxes than the aerosols. However,
75 they also noted that dust loadings are correlated to water vapor, so that their methodology
76 can not disentangle the relative effect of each other.

77 Identifying the physical mechanisms at play in North Africa during springtime, and
78 especially during heatwaves; describing their diurnal cycle evolution; their impact on the
79 surface energy budget and the near surface temperature therefore still need to be done. The
80 present study aims at filling these gaps, with a particular focus on the major heatwave of
81 April 2010. In line with these objectives, we will also present a new approach making use
82 of a specially-designed conceptual model that allows to isolate the radiative impact of water
83 vapor alone and therefore directly quantify its impact on the energy budget, distinctly from
84 the effects of aerosols and clouds.

85 This study shows that the 2010 heatwave is characterized by strong positive anomalies
86 of the daily-minimum temperatures and the incoming longwave fluxes over North Africa
87 by making use of several long-term observational datasets (satellite-based products and
88 ground-stations, described in section 2). It further explores the radiative impacts of clouds
89 and aerosols on 2m-temperatures (sections 3 and 4) and shows that, although strong positive
90 anomalies of AOD and cloud cover are found respectively over the Sahel and Sahara,
91 their radiative impacts are too weak to explain the anomalies of longwave fluxes and tem-
92 peratures. Boundary-layer physics is further explored with climate simulations performed
93 with the atmospheric component of the Centre National de Recherches Météorologiques
94 (CNRM) climate model, using a configuration in which the dynamics is nudged towards a
95 reanalysis (section 5). It shows that turbulence in the atmospheric surface layer and long-
96 wave radiation are the main drivers of the evolution of 2m-temperatures during the heat-
97 wave and that the longwave radiative coupling between the soil and the air surface layer
98 is strongly affected by the infrared emissivity of the atmosphere, which is in turn strongly
99 related to the 2m-specific humidity. Finally, a new and specially designed prognostic model
100 of surface-atmosphere radiative exchanges (hereafter called SARAWI) is presented. This
101 model is used to explore and quantify the impact of the radiative greenhouse effect of water
102 vapor on surface air temperature (section 6), and we introduce a Humidity Radiative Effect
103 (hereafter HRE) based on the model estimates. It shows that the heatwave is controlled by
104 the anomalously high specific humidity related to an early monsoon flux intrusion into the
105 Sahel, and to a coincident tropical plume into the Sahara. Conclusions are given in the final
106 section.

107 2 Data and methods

108 2.1 Surface temperature databases

109 This study makes use of the Berkeley Earth Surface Temperature gridded dataset, hereafter
110 referred to as BEST. This product uses the statistical Kriging method to interpolate data from
111 ground-based stations on a global regular $1^\circ \times 1^\circ$ grid [Rohde et al., 2013]. The dataset uses
112 2m-temperatures from an ensemble of weather stations compiled from 16 preexisting data
113 archives, among which the Global Historical Climatology Network (GHCN), and further
114 compiles data over 39000 ground-stations.

115 In the following, we use daily-minimum, daily-maximum and daily-average tempera-
116 tures T_{min} , T_{max} and T_{avg} which are available from 1880 to 2013, at a daily time scale.

117 For each grid point, we compute daily climatological values over the 2000-2013 period
118 (by averaging values for the 14 years and using a 21-days running-mean) for T_{min} , T_{max} and
119 T_{avg} . Hereafter, daily anomalies for 2010 are estimated from this 2000-2013 climatology
120 (this relatively short period, 2000-2013, was chosen for consistency with the analysis of the
121 satellite data presented below). We also compute, at each grid point, the daily 90% quantile

122 values of the temperature distributions built with the $21 \times 14 = 294$ values of the 21 calendar
123 days centered on the considered day and the 14 years of the 2000-2013 period.

124 We also used data from 222 SYNOP ground stations across North Africa archived by
125 the French weather service Météo-France.

126 2.2 The Clouds and the Earth's Radiant Energy System (CERES) database

127 We also use data from the Clouds and the Earth's Radiant Energy System (CERES) database,
128 developed by NASA [Wielicki et al., 1996, 1998], which are available from 2000 to 2017.
129 We use the SYN1DEG dataset, which is a level 3 satellite product which provides CERES-
130 observed radiative fluxes at 3-hourly and daily temporal resolution on a $1^\circ \times 1^\circ$ grid, together
131 with coincident Moderate Resolution Imaging Spectroradiometer (MODIS)-derived cloud
132 and aerosol properties, and geostationary-derived cloud properties and broadband fluxes
133 that have been carefully normalized with CERES fluxes. The use of measurements from a
134 constellation of geostationary orbiting satellites allows to more accurately model the vari-
135 ability between CERES Terra and Aqua satellite observations (cf [Doelling et al., 2013] for
136 a description of the methodology). This dataset also provides daily average $1^\circ \times 1^\circ$ grid-
137 ded data of cloud cover, total Aerosol Optical Depth at $0.55 \mu m$ (hereafter AOD), and total
138 column Precipitable Water (hereafter PW) estimated by MODIS.

139 We also use the Earth's surface computed upwelling and incoming shortwave (hereafter
140 SW_{in} and SW_{up}) and longwave (LW_{in} and LW_{up}) fluxes, for all-sky, clear-sky (cloud free) and
141 pristine (cloud and aerosol free, hereafter referred to as clean-sky) conditions. Surface fluxes
142 are provided with a 3 h timestep using a radiative transfer code ([Fu and Liou, 1992]) based
143 upon inputs from Terra and Aqua MODIS and 3-hourly geostationary data (for cloud and
144 aerosol properties), and meteorological assimilation data from the Goddard Earth Observing
145 System Model reanalyses (for meteorological profiles). Several sources of uncertainties arise
146 in these estimations of the daily surface fluxes. Rutan et al. [2015] evaluated them using 8
147 years of in-situ observations and concluded that downward fluxes have a bias of $3.0 W.m^{-2}$
148 in the shortwave and $-4.0 W.m^{-2}$ in the longwave. Results of the present study are given
149 within these uncertainties.

150 We compute local daily climatological values for all these fields over 2000-2013 in the
151 same way as done for BEST temperatures.

152 2.3 Automatic weather stations observations in the Sahelian Gourma (AMMA-CATCH)

153 The present study also uses ground-station measurements made in the Sahelian Gourma
154 (Mali), deployed at a site which belongs to the African Monsoon Multi-disciplinary Analysis
155 (AMMA)-CATCH network [Mougin et al., 2009].

156 In the following, we mostly focus on the measurement site of Agoufou, located in central
157 Sahel, at $15^\circ 20' 40'' N$ and $1^\circ 28' 45'' W$. Instruments are deployed in grassland, over sandy
158 soil, which is the dominant surface type in the Malian Gourma. An automatic weather station
159 (AWS) acquires data at a 15-min time step since April 2002, and provides air temperature,
160 relative humidity, rainfall, wind speed and direction as well as surface radiative and turbulent
161 fluxes.

162 The site is homogeneous over several kilometers, which allows a good estimate of the
163 radiative fluxes. These data have already been used for thermodynamic and climate analyses

164 by Guichard et al. [2009], Timouk et al. [2009], Roehrig et al. [2013] and Lohou et al. [2014]
165 among others.

166 2.4 CNRM-AM nudged simulation

167 In the present study, we use a simulation based on the atmospheric component of a proto-
168 type of the new CNRM climate model, hereafter referred to as CNRM-AM. This model is
169 based on the version 6.2.1 of the ARPEGE-Climat atmospheric model [Déqué et al., 1994;
170 Voldoire et al., 2013] and benefits from several significant and recently-implemented devel-
171 opments of the model physics parameterizations. This prototype version is similar to that
172 used in the recent studies of Michou et al. [2015]; Leroux et al. [2016]; Martin et al. [2017].

173 CNRM-AM is a major update of the CNRM-CM5 atmospheric component [Voldoire
174 et al., 2013]. It contains a prognostic turbulent kinetic energy (TKE) scheme [Cuxart et al.,
175 2000] that improves the representation of the dry boundary layer. The new convection
176 scheme represents in a unified way the dry, shallow and deep convective regimes, following
177 Guérémy [2011] and Piriou et al. [2007]. The convection scheme microphysics prognosti-
178 cally describes cloud liquid and ice water, as well as rain and snow specific masses following
179 the work of Lopez [2002]. It is also fully consistent with the microphysics scheme used for
180 the large-scale condensation and precipitation. Cloud macrophysics is handled by the Ri-
181 card and Royer [1993] scheme. The radiation scheme is based on the shortwave scheme of
182 Fouquart and Bonnel [1980] and on the longwave Rapid Radiation Transfer Model (RRTM,
183 [Mlawer et al., 1997]). An overview of the land surface model SURFEX can be found in
184 Masson et al. [2013] and more details on the physical content used in the present study
185 is described in Decharme et al. [2013, 2016]. SURFEX makes use of the ECOCLIMAP
186 database for surface parameters [Masson et al., 2003].

187 CNRM-AM is a spectral model that has been used here with a T127 truncation (about
188 1.4° resolution at the Equator). It has 91 vertical hybrid levels up to 80 km. The first model
189 level is near 12 m and the model has about 10 levels in the first atmospheric kilometer. It
190 is run in an Atmospheric Model Intercomparison Project (AMIP) configuration, in which
191 monthly-mean sea surface temperatures are prescribed and interpolated at each time step
192 of the model. The time step is 15 min. Monthly aerosol loadings are also prescribed and
193 constant across each month. A climatological annual cycle is used, which is computed
194 from the 1990-1999 period of a nudged AMIP simulation of CNRM-AM with the prognostic
195 aerosol scheme described in Michou et al. [2015]. Note that aerosol optical properties were
196 updated according to Nabat et al. [2013], compared to those used in CNRM-CM5.

197 Here, the main objective is to analyze the effects of the physical processes during the
198 April 2010 Sahelian heatwave, without the additional complexity induced by their interac-
199 tions with the large-scale dynamics. Therefore, a dynamical spectral nudging towards the
200 6-hourly ERA-interim reanalyzed fields [Dee et al., 2011] is applied to the wind vorticity
201 and divergence as well as to the surface pressure, which constrains the model to follow the
202 observed large-scale dynamical sequence [Coindreau et al., 2007]. The relaxation timescale
203 is 12h for the vorticity and 24h for the divergence and surface pressure. To let the model
204 physics adjust in the surface layer, the nudging is weakened at the first four model levels
205 (approximately up to 400 m above the ground), with no nudging at all at the first model level.
206 Note also that the simulation started on 1 January 1979 and ended on 31 December 2012,
207 so that the atmospheric and land-surface model spin-up can be neglected when focusing on
208 April 2010.

209 2.5 A conceptual prognostic model: The Surface-Atmosphere RAdiative Water vapor
210 Impact (SARAWI) model

211 A conceptual prognostic model has been specifically designed : The Surface-Atmosphere
212 RAdiative Water vapor Impact model (SARAWI). It is used in this study to investigate the
213 processes involved in the temperature fluctuations.

214 This conceptual model appears to be a useful tool to :

- 215 – Highlight the influence of physical processes. Hereafter, the impact of the water vapor
216 greenhouse effect is investigated, and the model allows to infer a Humidity Radiative
217 Effect (cf sections 6.3 to 6.5);
- 218 – Provide a simple-way to test the ability of new formulations of the physical processes
219 to correctly reproduce observations. For instance, hereafter, a linear regression of the air
220 emissivity is proposed in equation (9) and evaluated in section 6.1.
- 221 – Point out the biases and sources of uncertainty in state-of-the-art models and param-
222 eterizations (hereafter, when compared to the CNRM-AM model and observations, cf
223 sections 6.1, 6.2)
- 224 – Perform and interpret sensitivity tests in simple and unambiguous ways for a low com-
225 putational cost, contrary to complex GCM simulations (hereafter by modifying only the
226 longwave radiative effect of low-level humidity, cf sections 6.3, 6.4)).

227 2.5.1 Basic concepts and hypotheses

228 SARAWI consists of a simple model of the soil and lower atmosphere. It aims at investi-
229 gating the interactions at play between physical processes and the impact of their parame-
230 terizations on the evolution of the soil surface temperature T_s and of the surface-layer air
231 temperature T_a .

232 SARAWI assumes that turbulence and radiative transfer are the dominant terms ex-
233 plaining the evolution of T_s and T_a . The model solves local physical processes acting in the
234 boundary-layer (turbulence and radiation transfer) by decoupling them from the regional
235 and synoptic atmospheric processes that are either prescribed analytically or solved by an
236 external GCM-type model and prescribed into the SARAWI model. As shown in sections
237 5 and 6, these hypotheses are supported by the results given by the CNRM-AM simula-
238 tion, and our results suggest that this approach is sufficient to reproduce the spatial structure
239 and temporal evolution of the 2m-air temperature T_{2M} , at least over North Africa during
240 springtime 2010. The model can therefore be used to analyze the relative contributions of
241 regional-scale circulations versus local-scale processes.

242 In the SARAWI model, the soil and lower atmosphere are represented with two soil lay-
243 ers and one atmospheric layer, with the mass point of the atmospheric layer located at $\delta z/2$
244 above the ground, δz being the atmospheric layer depth. It can be used in a one dimensional
245 (1D) mode at a selected location, or over a given domain (hereafter all North Africa), as a
246 light 3D model, with vertical transfers only, explicitly represented across its three layers.

247 SARAWI solves three prognostic equations (one for the temperatures of each of the
248 three layers), together with a diagnostic equation for T_{2M} (details are given below). It makes
249 use of four additional equations for the physical parameterization of fluxes and tendencies,
250 combined with ten tuned or statistically-fitted parameterizations that account for physical
251 properties. Finally, simulations are performed with four external input fields.

2.5.2 SARAWI system of equations and parameterizations

Inputs: SARAWI makes use of four input fields, that can be prescribed analytically or from an atmospheric model. They are indicated in the “Inputs” field in Table 1.

Prognostic equations: SARAWI solves three prognostic equations for T_a , T_s and T_{2s} respectively the temperatures of the atmospheric layer, the soil surface layer and the deep soil layer. They are detailed in the “Prognostic equations” field of Table 1. The different terms on the right hand sides are detailed in the “Physical parameterizations” field.

Equation (1) is the classical thermodynamic equation in which we make the assumption that the effects of shortwave radiation, parameterized convection, large-scale condensation and precipitation, and advection are negligible in the atmospheric surface layer, so that the evolution of air surface temperature is mainly driven by longwave radiation and turbulence. We will show in section 5 that this hypothesis is supported by climate-model simulations.

Equations (2) and (3) follows a simple parameterization for a two-layers soil model, using the classical force-restore method of Noilhan and Planton [1989].

The last term on the right-hand side of equation (2) is proportional to a diffusive heat flux into the deep soil layer and tends to restore T_s to the mean soil temperature T_{2s} . C_s is the inverse of the soil heat capacity. In equation (2), the latent heat flux is assumed to be negligible, which is a realistic assumption over the Sahel and Sahara at the end of the dry season (cf section 5). Equations (2) and (3) introduce a relaxation time constant (τ) fixed at $\tau = 24\text{h}$, as in Noilhan and Planton [1989].

Physical parameterizations: Four physical parameterizations are used (cf equations (4) to (7) in Table 1). All parameters and variables present in equations (4) to (7) are detailed in Table 2.

Equations (4) and (5) correspond to classical formulations of the sensible heat flux and the net longwave flux at the surface (e.g. [Noilhan and Planton, 1989]).

The longwave radiation warming of the atmospheric layer is given by equation (6), which is a simplification of the longwave model of Mlawer et al. [1997] corresponding to a radiative balance within the atmospheric layer. Its first term corresponds to the infrared absorption by the atmospheric layer of the emitted infrared flux from the surface, and its second corresponds to the emitted infrared flux toward the surface combined with the absorbed part of that same flux reflected over the soil surface. The coefficient h_{rad} is a radiative scale height (see Table 2 and section 2.5.3), which represents the height of the layer radiatively affected by the surface, in the sense that the upwelling longwave at the surface LW_{up} is absorbed within the layer of height h_{rad} , and respectively that no longwave radiation emitted from above that layer reaches the soil surface without being absorbed. The introduction of h_{rad} in equation (6) makes explicit that the transmitted incoming longwave radiation at the surface issued from above the altitude h_{rad} can be neglected.

The turbulent processes are parameterized with equation (7), which is a simplification of the Mellor and Yamada [1982] turbulence scheme for a one-layer atmospheric model. The first term corresponds to a turbulent exchange with the soil surface layer and the second to a turbulent exchange with the air above the atmospheric layer.

Diagnostic equation for T_{2m} : The 2m-air temperature T_{2m} is diagnosed with a linear interpolation between the soil surface temperature T_s and the air layer temperature T_a , given by equation (8), as usual in atmospheric model. The coefficient c_{12m} typically depends on

296 the static stability of the atmosphere. Here, we parameterize this coefficient according to
 297 Mahfouf et al. [1995].

INPUTS		
(a)	SW_{net}	Net shortwave flux at the surface
(b)	hus	Specific humidity at the atmospheric level
(c)	V_a	Wind speed at the atmospheric level
(d)	T_{2a}	Temperature of the air above the SARAWI atmospheric layer (used in the parameterization of turbulence only)
PRONOSTIC EQUATIONS		
(1)	$\frac{\partial T_a}{\partial t} = \frac{\partial T_a}{\partial t}_{rlw} + \frac{\partial T_a}{\partial t}_{pbl}$	Atmospheric layer temperature (T_a) equation
(2)	$\frac{\partial T_s}{\partial t} = C_s \cdot (SW_{net} + LW_{net} - H) - \frac{2\pi}{\tau} (T_s - T_{2s})$	Soil surface layer temperature (T_s) equation
(3)	$\frac{\partial T_{2s}}{\partial t} = \frac{1}{\tau} (T_s - T_{2s})$	Deep soil layer temperature (T_{2s}) equation
PHYSICAL PARAMETERIZATIONS		
(4)	$H = \rho \cdot C_p \cdot C_h \cdot V_a \cdot (T_s - T_a)$	Surface sensible heat flux parameterization
(5)	$LW_{net} = \sigma \cdot (\epsilon_a \cdot T_a^4 - \epsilon_s \cdot T_s^4)$	Surface net longwave flux parameterization
(6)	$\frac{\partial T_a}{\partial t}_{rlw} = \frac{\sigma}{\rho \cdot C_p \cdot h_{rad}} \cdot \{\epsilon_a \cdot \epsilon_s \cdot T_s^4 - [1 - \epsilon_a(1 - \epsilon_s)] \cdot \epsilon_a \cdot T_a^4\}$	Longwave tendency parameterization
(7)	$\frac{\partial T_a}{\partial t}_{pbl} = K_s \frac{V_a (T_s - T_a)}{\delta z} + K_h \frac{T_{2a} - T_a}{\delta z \cdot h_{turb}}$	Turbulent tendency parameterization
DIAGNOSTIC EQUATIONS		
(8)	$T_{2m} = T_s + c_{t2m} \cdot T_a$	2m-air temperature diagnostic

Table 1 The system of equations and parameterizations of the SARAWI pronostic model.

298 2.5.3 Physiographic and physical parameters

299 In equations (3) to (8), ten parameters have to be tuned, prescribed or parameterized: τ , ϵ_s ,
 300 ϵ_a , C_s , h_{rad} , h_{turb} , C_h , K_s , K_h and c_{t2m} .

301 Among those parameters, ϵ_s and C_s are local physiographic properties dependent on
 302 ground cover and soil texture. They have to be prescribed using soil surface characteristics

303 databases. C_s has a major importance since it strongly modulates the diurnal soil and air
 304 temperature ranges. ϵ_s is typically very close to 1.

305 h_{rad} , h_{urb} , C_h , K_s and K_h have to be tuned or statistically fitted, and c_{t2m} requires a
 306 parameterization.

307 For ϵ_a , we propose an original and simple approach. While longwave radiative fluxes
 308 directly depends on temperature through the Stefan-Boltzman's law, longwave emissivity
 309 ϵ_a (and fluxes) also varies with atmospheric water vapor (e.g. [Prata, 1996]). Since the
 310 SARAWI model has been mainly designed (and will be used hereafter) to evaluate the ra-
 311 diative impacts of water vapor, it appears crucial that the parameterized infrared emissivity
 312 be sensitive to its variations. Similarly to Herrero and Polo [2012], we propose a simple
 313 parameterization based on a multiple linear regression:

$$\epsilon_a = a_1 + a_2.hus + a_3.T_a \quad (9)$$

314 Table 2 synthesized the fixed values or parameterizations used in the SARAWI model.
 315 Note that this could be easily modified in other versions of the model in order to improve
 316 some representations of these parameters or to adjust them to other areas of the globe.

317 Appendix A gives details on the reasons for using values and parameterizations given in
 318 Table 2, the methodology used to infer those values and some uncertainties as compared to
 319 other parameterizations.

320 2.5.4 Configuration of the SARAWI simulations

321 In the present study, SARAWI simulations are made for April 2010 over North Africa, be-
 322 tween 0° and 30°N in latitude and between 20°W and 20°E in longitude. The depth of the
 323 atmospheric layer is $\delta z = 25\text{m}$, the horizontal resolution is fixed to $1.4^\circ \times 1.4^\circ$ and the time
 324 step is 15-min, in order to compare results to CNRM-AM simulations.

325 The simulations are initialized using T_a and T_s from the CNRM-AM simulation on 1st
 326 April; and T_{2s} is assumed to be equal to T_s at the first time step (in practice, after the spin-up
 327 period, which lasts less than 24h, the precise choice of the initial field of T_{2s} has no influence
 328 on our results).

PHYSIOGRAPHIC AND PHYSICAL PARAMETERS		
Variable	Description	Fixed value or parameterization used
ρ	Air density	$\rho = 1.2 \text{ kg.m}^{-3}$
C_p	Air specific heat capacity	$C_p = 1004 \text{ J.kg}^{-1}.K^{-1}$
σ	Stefan-Boltzman constant	$\sigma = 5.67 * 10^{-8} \text{ W.m}^{-2}.K^{-4}$
τ	Relaxation time constant	$\tau = 24 \text{ h}$ (Force-restore approach of Noilhan and Planton [1989])
ϵ_s	Soil surface total infrared emissivity	$\epsilon_s = 0.9946$ North African average, extracted from the ECOCLIMAP database ([Champeaux et al., 2005; Faroux et al., 2013])
ϵ_a	Air total infrared emissivity	$\epsilon_a = a_1 + a_2.hus + a_3.T_a$ $a_1 = 0.667, a_2 = 1.17.10^{-2}$ with hus in g/kg and $a_3 = 4.55.10^{-4}$ with T_a in $^{\circ}C$.
C_s	Inverse of the soil heat capacity	Extracted from the ECOCLIMAP database ([Champeaux et al., 2005; Faroux et al., 2013]). Averaged over daytime and nighttime : $C_s^{night}(lon, lat)$ and $C_s^{day}(lon, lat)$.
h_{rad}	Radiative scale height	$h_{rad} = c_{rad}.\delta z$, with $c_{rad} = 4.74$
h_{turb}	Turbulent scale height	$h_{turb} = \delta z_2 = 35m$
C_h	Drag coefficient	Daytime $C_h = 4.10^{-3}$. Nighttime : $C_h = 5.10^{-4}$.
K_s	Turbulent drag coefficient	Daytime : $K_s = 1.6.10^{-4}$. Nighttime : $K_s = 2.10^{-5}$.
K_h	Turbulent diffusivity	Daytime : $K_h = 0.94 \text{ m}^2.s^{-1}$. Nighttime : $K_h = 0.08 \text{ m}^2.s^{-1}$.
c_{r2m}	Static stability dependent coefficient	Based on Mahfouf et al. [1995].

Table 2 The physiographic and physical parameters used by the SARAWI pronostic. More details are given in appendix A.

329 3 Observed large-scale features on spring 2010

330 In this section, we make use of the previously described long-term observational datasets
331 to show that the 2010 heatwave is characterized by strong positive anomalies of the daily-
332 minimum temperatures and the incoming longwave fluxes over North Africa, correlated with
333 positive anomalies of precipitable water.

334 3.1 Maps of April 2010 anomalies

335 In the present study, we refer to ‘‘North Africa’’ to describe the geographic region of Africa
336 located between $0^{\circ}N$ and $30^{\circ}N$; $20^{\circ}W$ and $20^{\circ}E$. Hereafter, two subregions of interest are
337 defined : The Sahel, as the area between $14^{\circ}N$ and $18^{\circ}N$; and the Sahara, between 18° and
338 $30^{\circ} N$. Both of these subregions extend from $20^{\circ}W$ to $20^{\circ}E$.

339 Figure 1 shows April 2010 monthly means and monthly anomalies of BEST T_{min} and
 340 T_{max} , CERES LW_{in} , SW_{in} , cloud cover fraction, AOD and PW.

341 In April 2010, T_{min} and T_{max} exhibit a springtime pattern with a maximum temperatures
 342 latitudinal band centered on the Sahel (see Figure 1a). Similarly, the maximum of LW_{in} is
 343 localized over the Sahel. SW_{in} , cloud cover and PW exhibit distinct patterns characterized
 344 by strong meridional gradients. This highlights the contrast between the Sudano-Guinean
 345 region (south to 14° N) affected by the moist monsoon flow associated with clouds and re-
 346 duced SW_{in} ; and the Sahel and the Sahara subregions (see Figure 1a) with stronger SW_{in} ,
 347 reduced cloud cover and enhanced dryness (low PW). The AOD pattern emphasizes a maxi-
 348 mum over Mali, Niger and South Algeria, which are dominantly affected by dust events due
 349 to the combination of strong winds, low surface roughness, dry soils and sporadic vegetation
 350 in springtime.

351 Strong positive temperatures anomalies (up to 3 or 4° C) are observed in the Sahel and
 352 Sahara, particularly strong over Mauritania, Algeria and Mali. T_{min} anomalies are stronger
 353 and impact a wide area, covering the western and central Sahel and Sahara (Figure 1b,d).
 354 These regions corresponds to enhanced LW_{in} in April 2010, strong compared to the clima-
 355 tology, reaching anomalies of about 30 to 40 W/m^2 (Figure 1h). A strong negative SW_{in}
 356 anomaly is also observed in the Sahel and Sahara, with a similar pattern to that of the LW_{in}
 357 positive anomaly (Figure 1f).

358 Strong positive anomalies of cloud cover, AOD and PW also occur over the Sahel and
 359 Sahara in April 2010 (Figure 1j,l,n). The cloud cover increase mainly concerns the northern
 360 Sahara and is mostly related to enhanced high-level clouds (not shown). These anomalies
 361 are due to a tropical plume event, common in North Africa during spring [Knippertz and
 362 Martin, 2005; Fröhlich et al., 2013]. The tropical plume enhanced PW over Mauritania,
 363 Algeria and Libya and favored the occurrence of high clouds and low-level water vapor. PW
 364 is also increased over Mali and Burkina Faso, as the monsoon flow is anomalously north
 365 during this period. Strong AOD anomalies are located over Mali and Niger and are caused
 366 by several dust events.

367 3.2 Climatological and 2010 springtime evolution

368 In the following, two main climatological areas are considered: The Sahara and the Sahel,
 369 defined in the previous section. They both extend over the longitude band $[20^{\circ}\text{W}, 20^{\circ}\text{E}]$ and
 370 only account for land pixels (Figure 1a).

371 Figure 2a,b presents the climatological and 2010 time series of T_{min} , T_{avg} and T_{max} given
 372 by BEST and averaged over each of these two areas. The 2010 springtime (March-April-
 373 May) exhibits relatively strong positive temperature anomalies, reaching 1.30°C and 1.29°C
 374 for T_{min} and T_{max} respectively, on average over the Sahara; and 1.26°C and 0.96°C on av-
 375 erage over the Sahel (to be compared to a mean springtime 90% quantile value which is
 376 respectively 3.06°C , 3.59°C , 2.66°C and 2.69°C above the climatology). Over the Sahel,
 377 they occur close to their climatological annual maximum, which leads to particularly high
 378 raw temperatures.

379 CERES incoming radiation fluxes SW_{in} and LW_{in} are averaged over each domain (Figure
 380 2c,d,e,f). Daily incoming longwave fluxes are significantly higher than shortwave fluxes
 381 (about 120 W/m^2 on average over the period). The variability of SW_{in} is driven by cloud
 382 cover and AOD fluctuations, which leads to strong synoptic and day-to-day modulations in
 383 the Sahel (Fig. 2d) whereas LW_{in} corresponding variability is weaker (Fig. 2f).

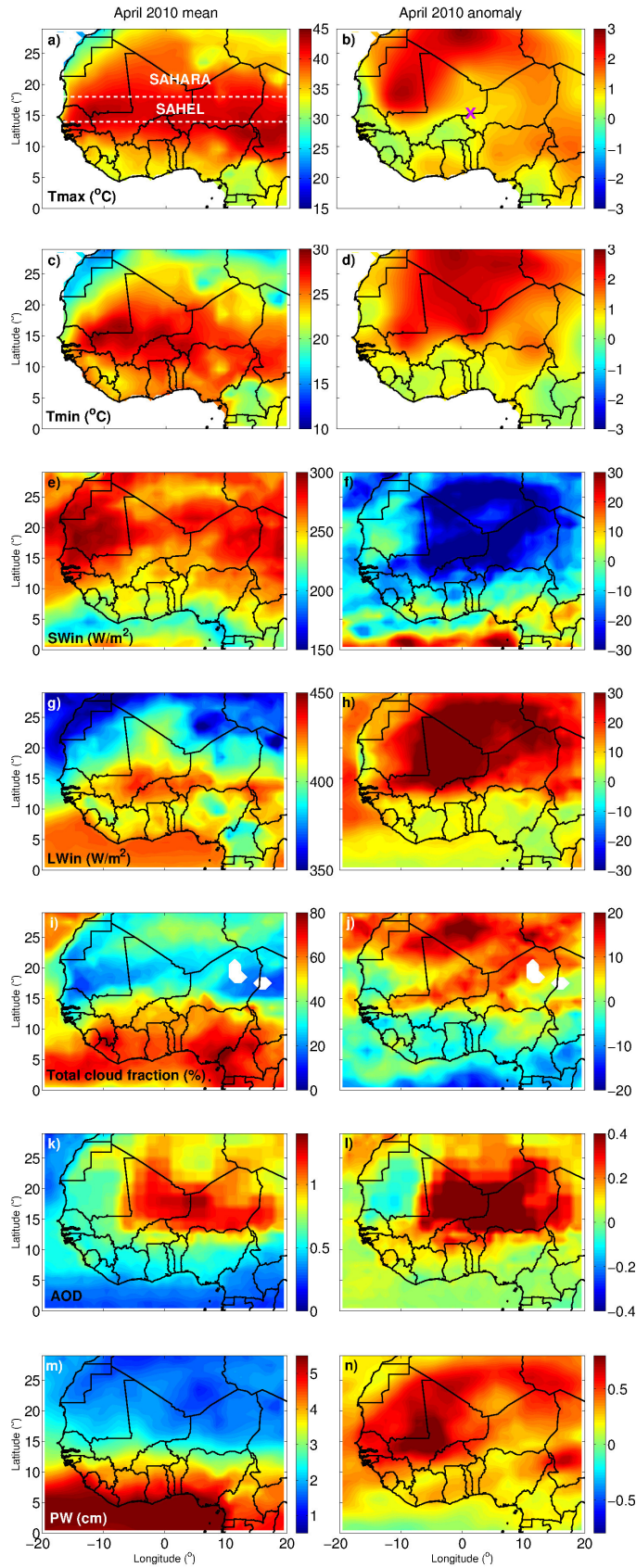


Fig. 1 Monthly-mean (left) and climatological anomalies (right) for April 2010 of T_{max} (a,b), T_{min} (c,d), SW_{in} (e,f) and LW_{in} (g,h) total cloud cover fraction (i,j), Aerosol Optical Depth (k,l) and Precipitable Water (m,n). White dotted lines in panel a) delimitates Sahel and Sahara as defined in this study. Purple cross in panel b shows the location of the Agoufou station.

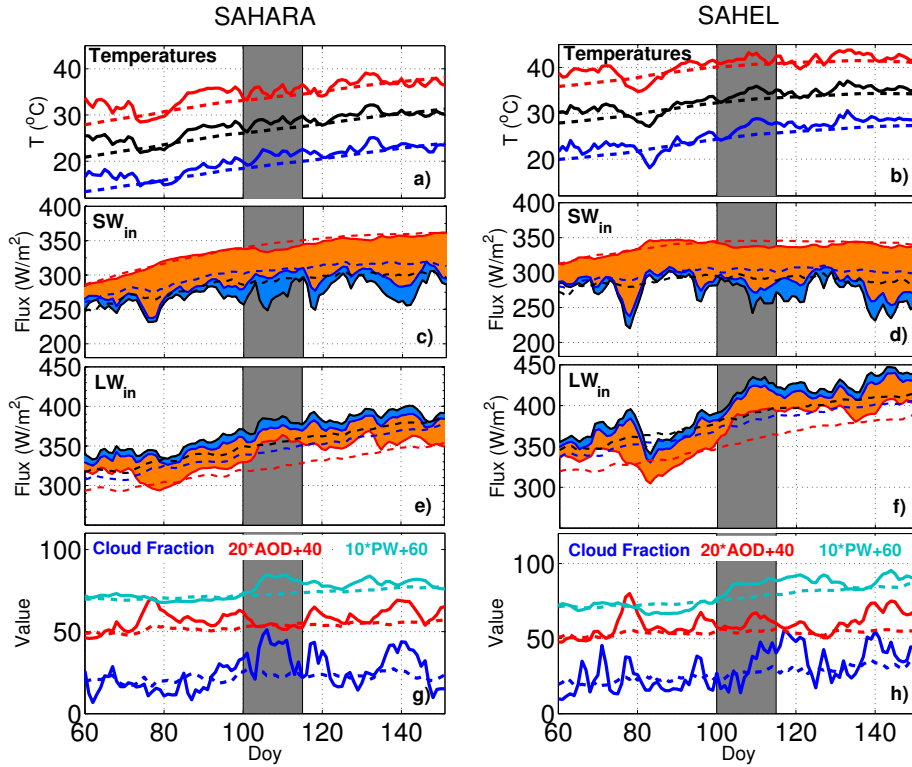


Fig. 2 Springtime time series of (a,b) T_{min} (blue), T_{avg} (black) and T_{max} (red); (c,d) daily-average SW_{in} (black), clear-sky SW_{in}^{clear} (blue), clean-sky SW_{in}^{clean} (red); blue shading therefore corresponds to the Cloud Radiative Effect and orange shading to the Aerosol Radiative Effect (see section 4.1 for more details); (e,f) same as (c,d) for incoming longwave fluxes; and (g,h) Cloud fraction (in %, blue), $20 \cdot AOD + 40$ (red), $10 \cdot PW + 60$ (in cm, light blue). All values correspond to the average over the Sahara (left) or the Sahel (right). Solid lines : 2010 time series. Dashed lines : climatological time series. Grey shading : April 2010 Heatwave period.

384 SW_{in} anomalies, are persistently negative, near $-15 W/m^2$ on average over springtime
 385 for both domains. In contrast, LW_{in} anomalies are mostly positive during the period, reaching
 386 about $+18.5 W/m^2$ on average over springtime for both domains.

387 These anomalies are consistent with the increased cloud cover, AOD and PW observed
 388 during the period (Figure 2g,h). Variations of SW_{in} are strongly coupled with the variations of
 389 cloud cover. Likewise, $SW_{in}^{clear-sky}$ is strongly related to AOD. By contrast, the fluctuations
 390 of LW_{in} appear more strongly related to those of PW. These correlations are even more
 391 pronounced when restricted to the heatwave period (grey shading on Figure 2) that is further
 392 discussed in the next subsection.

3.3 Focus on the heatwave period

Recently, Barbier et al. [2018] developed a methodology to detect and track heatwaves over West Africa as intraseasonal events. They detect heatwaves when temperature intraseasonal anomalies exceed the 90% percentile of their local climatological distribution over a sufficiently extended area (greater than $6.10^5 km^2$) for at least 3 consecutive days. For 2010, several heatwaves were identified when applying this methodology over the domain considered in the present study ($[20^\circ W, 20^\circ E]$, $[0^\circ N, 30^\circ N]$) (e.g. Day Of Year (DOY) 60-75, 100-115, 125-135, see also Figure 2 in Barbier et al. [2018]). In the following, we focus on the heatwave event which occurred between 10 and 25 April, i.e. DOY 100 and 115. A significant part of the domain (about $24.10^5 km^2$, i.e. 20% of the domain) was affected by this long-lasting event and furthermore, it occurred when temperatures were very high over the Sahel (Fig. 2b). Hereafter, this period is referred to as the heatwave period (HW, grey shading in Figures). Note that the details of physical processes and mechanisms at play during springtime North African heatwaves are likely to vary from one event to another; in particular when considering late winter events (occurring in a very dry environment) or early monsoon events in late June (when the atmospheric water amount is on average higher). The period on which we focused here is more representative of North African heat waves occurring during the spring period when temperatures reach their annual maxima in the Sahel.

Increased T_{min} and T_{max} (and therefore T_{avg}) anomalies occur during this heatwave period, up to $4^\circ C$ over both the Sahel and Sahara. They coincide with reduced SW_{in} (anomalies up to $-49W/m^2$) and strongly enhanced LW_{in} (anomalies up to $+44W/m^2$). Note that the heatwave more strongly affects T_{min} , and is slightly stronger over the Sahara.

Temporal correlation coefficients between all the fields shown in Figure 2, both during the heatwave and pre-heatwave periods, are indicated in Table 3. Whereas all these fields display marked anomalies during the heatwave, day-to-day fluctuations are strongly positively correlated ($r > 0.8$ on both the Sahel and Sahara) only between T_{min} and LW_{in} , T_{min} and PW, LW_{in} and PW; (see bold values in Table 3). This suggests a tight link between nighttime temperatures, incoming longwave fluxes and precipitable water, both over the Sahel and Sahara, while every other covariations are less relevant. Note that during the pre-heatwave 40 days springtime period, these three correlations are significantly lower than during the heatwave period. This is particularly true over the Sahara where the strong link between PW and LW_{in} or T_{min} appears to be limited to the heatwave period. This highlights the impact of humidity during the heatwave, that will be further explored with the CNRM-AM and SARAWI models in section 5 and 6. Table 3 also highlights that cloud cover has a direct influence on the reduction of SW_{in} , which is expected.

Positive correlations are also found between cloud cover and LW_{in} (or T_{min}), on average over both the Sahel and Sahara. Similarly, a significant positive correlation is found between AOD and LW_{in} (or T_{min}), but only over the Sahel (the correlation being negative over Sahara). However, these correlations should be interpreted with care. Indeed, cloud and aerosol longwave effects, that will be further explored in section 4, will be shown to be unable to explain LW_{in} anomalies. Rather, these correlations are explained by covariations between PW and cloud cover (correlation of about 0.65), and between AOD and cloud cover over the Sahel (correlation of 0.74, due to the occurrence of dust events in Eastern Sahel and cloud intrusions in Western Sahel at the same time, not shown).

T_{max} fluctuations are not easily related to either incoming radiation fluxes, clouds, PW or aerosols. They are positively correlated with SW_{in} over the Sahara, while - suprisingly - negatively correlated over the Sahel during the heatwave. T_{max} fluctuations are also negatively correlated with cloud cover and AOD over Sahara, but positively over the Sahel. This

441 suggests that T_{max} variations are probably explained by a complex interplay between various
 442 processes operating at different scales.

443 In summary, the April 2010 heatwave emerges from the climatology mainly because of
 444 the very high T_{min} prevailing during this 15-day period, while high T_{max} are restricted to a
 445 shorter duration (10 days) with weaker departure from the 90% percentile threshold. In the
 446 following, we focus mainly on the understanding of T_{min} anomalies.

Couples of variables	HEATWAVE		PRE-HEATWAVE	
	SAHEL	SAHARA	SAHEL	SAHARA
T_{min} and LW_{in}	0.97 (0.94)	0.85 (0.74)	0.74	0.87
T_{min} and SW_{in}	-0.84 (-0.86)	0.01 (-0.46)	-0.20	0.55
T_{min} and AOD	0.82 (0.87)	-0.73 (-0.57)	0.22	-0.09
T_{min} and Cloud cover	0.77 (0.64)	0.37 (0.62)	0.16	0.59
T_{min} and PW	0.84 (0.74)	0.85 (0.76)	0.60	0.11
T_{max} and LW_{in}	0.62 (0.47)	0.22 (-0.09)	0.24	0.73
T_{max} and SW_{in}	-0.43 (-0.23)	0.53 (0.30)	0.43	0.76
T_{max} and AOD	0.59 (-0.39)	-0.69 (-0.45)	-0.40	-0.24
T_{max} and Cloud cover	0.25 (-0.03)	-0.30 (-0.24)	0.01	0.43
T_{max} and PW	0.36 (0.15)	0.25 (-0.04)	0.29	-0.09
LW_{in} and AOD	0.82 (0.85)	-0.62 (-0.31)	0.69	0.28
LW_{in} and Cloud cover	0.75 (0.49)	0.70 (0.93)	0.55	0.67
LW_{in} and PW	0.87 (0.82)	0.95 (0.86)	0.72	0.11
SW_{in} and AOD	-0.91 (-0.92)	-0.31 (-0.24)	-0.80	-0.33
SW_{in} and Cloud cover	-0.82 (-0.72)	-0.82 (-0.87)	-0.57	0.07
SW_{in} and PW	-0.66 (-0.61)	-0.16 (-0.44)	-0.49	-0.37

Table 3 Correlation coefficient r between two fields given in the left column over the Sahel (columns 2 and 4) and the Sahara (columns 3 and 5) during the heatwave period (10 to 25 April, column 2 and 3) and during the pre-heatwave springtime period (1 March to 10 April, columns 4 and 5). Values in parentheses are the correlation coefficient in terms of anomalies instead of raw values. Strongest correlations ($|r| > 0.8$ on both domains) are underlined with bold characters.

447 3.4 Significant LW_{in} positive anomalies in T_{min} heatwave areas

448 The previously described strong positive correlation between daily-mean values of LW_{in} and
 449 T_{min} (or their anomalies, cf Table 3) remains true at different time scales: spatially-averaged
 450 over the Sahel and Sahara, the correlation coefficient reaches $r = 0.99$ over the annual cycle,
 451 0.96 over springtime and 0.90 over April 2010. This correlation can be further analyzed in
 452 space with Figure 3, which shows LW_{in} anomalies for each day of the heatwave, overlaid by
 453 areas affected by the T_{min} -heatwave (in black contours). Strong T_{min} positive anomalies tend
 454 to overlay strong LW_{in} positive anomalies (up to $44W/m^2$), both over the Sahel and Sahara.

455 This relationship is however weaker over the Sudano-Guinean area, south to $12^\circ N$,
 456 which is the approximate location of the InterTropical Discontinuity (ITD) during spring-
 457 time. There, T_{min} can reach anomalously-high values, with moderate LW_{in} anomalies (despite
 458 high LW_{in} raw values). This suggests that surface incoming longwave fluxes in the moister
 459 and wetter April Sudano-Guinean climate are less sensitive to fluctuations of water vapor
 460 and cloud cover than the driest April climate of Sahel and Sahara, in agreement with e.g.
 461 Stephens et al. [2012].

462 This also points out to distinct processes and mechanisms leading to heatwaves in the
 463 Sudano-Guinea region, while the link with LW_{in} clearly dominates in the Sahel and Sahara.
 464 Hereafter, we focus on the Sahel and Sahara.

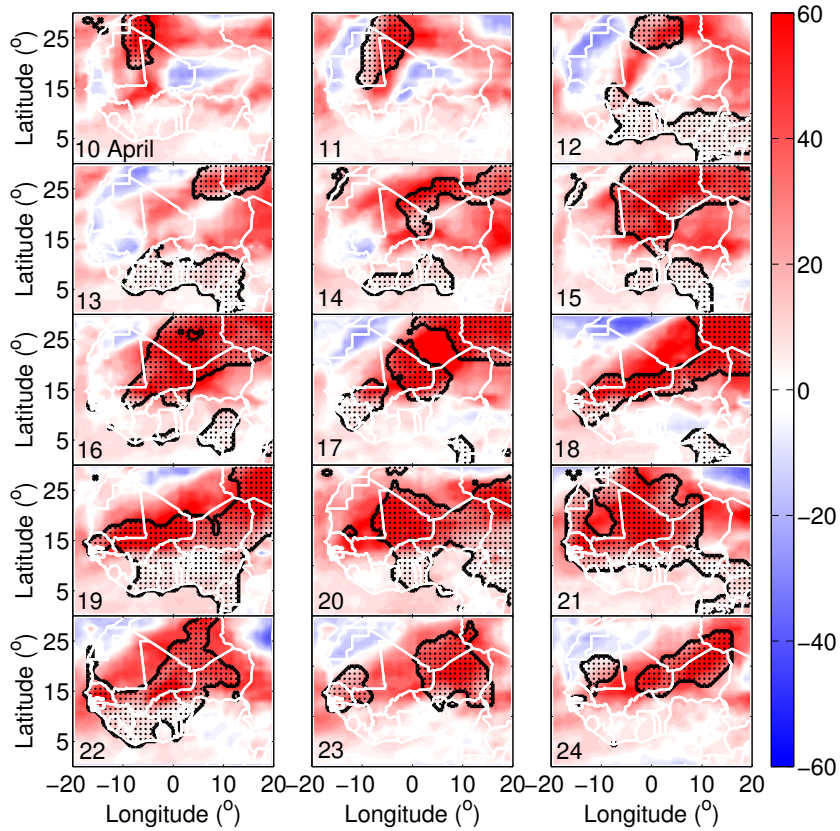


Fig. 3 Maps of the anomalies of the CERES daily incoming longwave flux, LW_{in} (color shading) superimposed with the areas affected by the heatwave, i.e. where T_{min} exceeds its local daily 90% percentile threshold (black dots), from 10 to 24 April 2010.

465 **4 Cloud and aerosol radiative effects**

466 Here, we explore the radiative impacts of clouds and aerosols and show that, although strong
 467 positive anomalies of AOD and cloud cover are found respectively over the Sahel and Sa-
 468 hारा, their radiative impacts are too weak to explain the anomalies of longwave fluxes.

469 4.1 Quantification of the Cloud Radiative Effect (CRE) and Aerosol Radiative Effect 470 (ARE)

471 For any radiative flux F , the CERES database provides an estimate of the corresponding
 472 clear-sky (ie cloud free) $F_{clear-sky}$ and clean-sky (ie cloud and aerosol free) $F_{clean-sky}$ com-
 473 puted fluxes.

474 Following the definition of Ramanathan et al. [1989], the Cloud Radiative Effect (CRE)
475 can be expressed as:

$$CRE = F - F_{clear-sky} \quad (10)$$

476 and similarly for the Aerosol Radiative Effect (ARE):
477

$$ARE = F_{clear-sky} - F_{clean-sky} \quad (11)$$

478 The Total Radiative Effect (TRE) is then:

$$TRE = CRE + ARE \quad (12)$$

479 4.2 Daily Radiative Effects during the heatwave

480 Figure 4 illustrates the daily-mean CRE and ARE in both the shortwave and longwave bands
481 for 15 April 2010, i.e. day 105.

482 That day, the total cloud fraction is high over the northern Sahara, and the AOD is
483 particularly strong over Niger, Eastern Mali and Southern Algeria (Figure 4a,b).

484 Cloud cover and dust loadings both reduce incoming shortwave radiative fluxes at the
485 surface, leading to negative shortwave CRE and ARE (Figure 4c,d). In contrast, the incom-
486 ing longwave radiative flux at the surface is increase below clouds and high dust loadings,
487 leading to positive CRE and ARE, up to several tens of W/m^2 in these areas (Figure 4e,f).
488 This emphasizes how both aerosols and clouds can have a strong radiative impact over West
489 Africa in spring.

490 4.3 Day-to-day evolution of ARE and CRE during the heatwave

491 On average over both the Sahel and the Sahara, raw values of ARE are stronger than CRE
492 both in the shortwave and longwave bands (Figure 5). SW_{in} is reduced by about $20W/m^2$
493 with clouds and by another $50W/m^2$ with dust loadings. Conversely, LW_{in} is increased by
494 about $10W/m^2$ with clouds and by another $25W/m^2$ with dust loadings.

495 During the whole spring 2010, large negative anomalies of shortwave ARE and positive
496 anomalies of longwave ARE are observed, both over the Sahel and Sahara (Figure 5). This
497 is consistent with the positive anomaly of AOD (red curves in Figure 2g,h) that increases
498 both shortwave cooling and longwave warming. A few strong dust events occur during this
499 period, for instance between DOY 75 and 80, when ARE reduces SW_{in} by $-90W/m^2$ and
500 increases LW_{in} by $+55W/m^2$ over the Sahel. The heatwave period (grey shading in Figure
501 5) is however less affected by the ARE over the Sahara (with anomalously low values in the
502 longwave) and only slightly affected by a positive ARE anomaly over the Sahel, at the end
503 of the period, between DOY 110 and 115.

504 Clouds have a lower radiative impact, both on longwave and shortwave fluxes, and the
505 only significant CRE negative anomaly is observed in the shortwave over Sahara during the
506 heatwave (where it is driven by the tropical plume event) and over the Sahel at the end of
507 the heatwave period. The longwave CRE remains close to its climatological values, without
508 any notable anomaly during the heatwave.

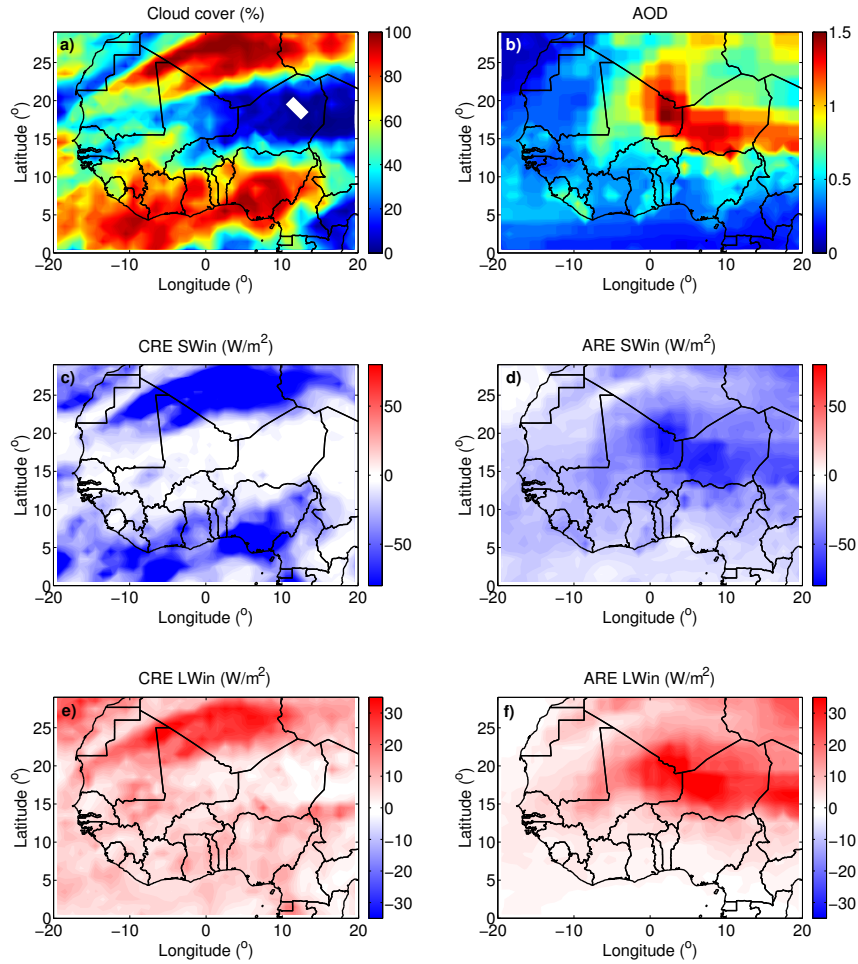


Fig. 4 Cloud cover area (%) (a) and AOD (b), CRE (c) and ARE (d) for SW_{in} (in W/m^2), CRE (e) and ARE (f) for LW_{in} (in W/m^2), over North Africa given by CERES on 15 April 2010, i.e. doy 105.

509 4.4 Cloud and Aerosol contributions to radiative anomalies

510 The ARE and CRE anomalies, together with the resulting TRE anomalies are compared to
 511 the incoming radiative flux anomalies in Figure 6. For each region, the fraction of the in-
 512 coming flux anomalies explained by either clouds or aerosols or the combination of the two
 513 is analyzed. Note that, since clouds reduce SW_{in} (cf Figure 5), a negative (respectively posi-
 514 tive) anomaly of shortwave CRE does not correspond to a lower *radiative impact*, but means
 515 that clouds produce a *stronger reduction* (respectively a lower reduction) of the incoming
 516 fluxes in 2010 than usual at the same day. Similarly, since clouds increase LW_{in} , a positive
 517 (resp. negative) anomaly of longwave CRE means that clouds produce a stronger increase

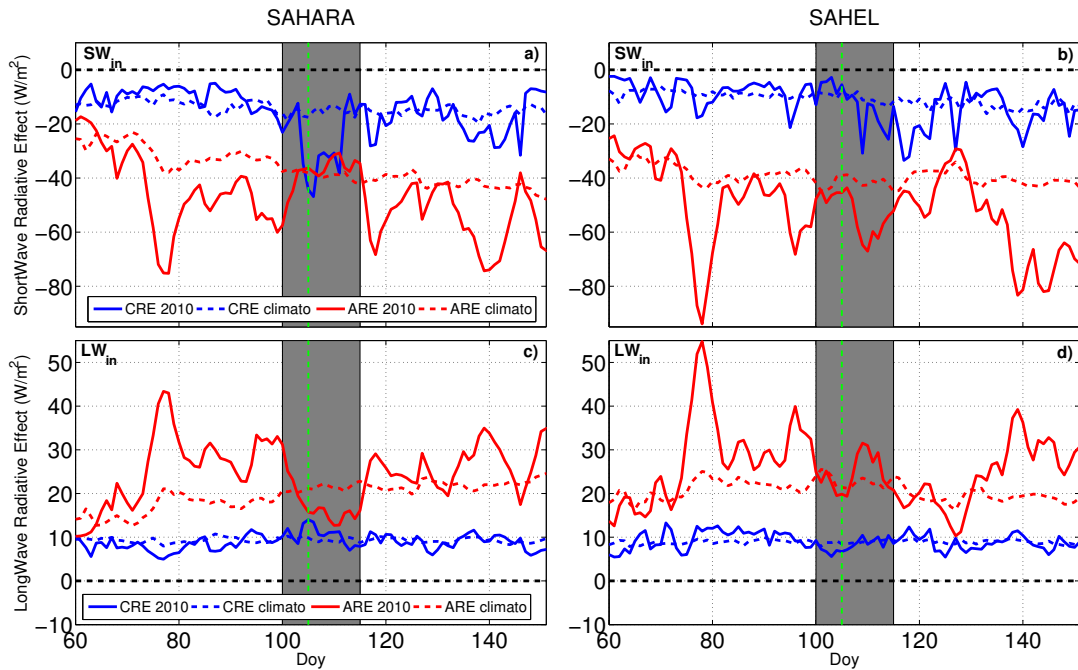


Fig. 5 springtime time series of incoming shortwave (a,b) and longwave (c,d) ARE (red) and CRE (blue), spatially averaged over the Sahara (left) and the Sahel (right). Solid lines: 2010. Dashed lines: climatology. The vertical dashed green line indicates 15 April 2010, shown in Figure 4.

518 (resp. a lower increase) of the incoming fluxes in 2010 than usual at the same day. Same
 519 conclusions can be dressed for ARE.

520 During the heatwave, a strong negative anomaly of SW_{in} is observed (Figure 6a,b). It is
 521 almost entirely explained by clouds over the Sahara, and by a combined effect of clouds and
 522 aerosols in the Sahel (with a larger contribution from aerosols though). Note that the 15-day
 523 period following the heatwave is also marked by a strong negative anomaly of SW_{in} , which,
 524 in contrast, is almost entirely explained by aerosols in the Sahara.

525 The heatwave is characterized by a wide and strong positive anomaly of LW_{in} (about
 526 $25W/m^2$ in the Sahara and $30W/m^2$ in the Sahel, cf Figure 6c,d). CERES surface radiative
 527 fluxes estimates do not support that clouds and aerosols might drive this positive anomaly,
 528 as they even contribute to a negative anomaly over the Sahara and to a very weak ARE
 529 positive anomaly of $1.5W/m^2$ over the Sahel, which roughly corresponds to only 5% of the
 530 total LW_{in} anomaly. Conversely, this anomaly of LW_{in} is strongly correlated to that of PW
 531 (Table 3 and Figure 6e,f), which suggests that the radiative effect of water vapor contributes
 532 to the emergence of this LW_{in} anomaly. This water vapor radiative effect will be further
 533 investigated in details with the SARAWI model in section 6.

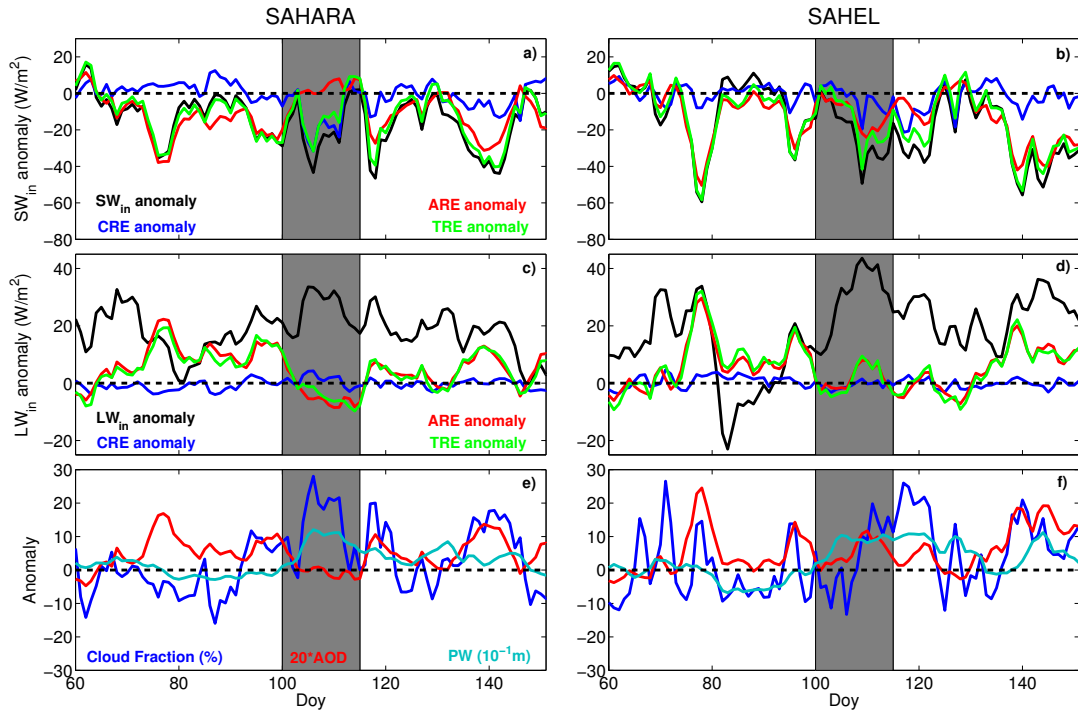


Fig. 6 springtime time series of anomalies of: shortwave fluxes and shortwave ARE, CRE, TRE (a,b), longwave fluxes and longwave ARE, CRE, TRE (c,d), cloud fraction, AOD and PW (e,f), averaged over the Sahara (left) and the Sahel (right).

534 5 Nudged climate model simulation results

535 In this section, boundary-layer physics is explored using climate simulations performed with
 536 CNRM-AM. We show that the 2m-temperature is driven by turbulence and longwave radi-
 537 ation, and that the latter drives its nighttime evolution. Atmospheric longwave emissivity is
 538 found to be closely related to 2m-specific humidity.

539 5.1 Maps of fluxes and temperature during the heatwave

540 The dynamical nudging towards ERA-interim fields prevents strong departures of the CNRM-
 541 AM simulation from observations and allows to follow the realistic chronology of the heat-
 542 waves events. Indeed, the annual cycles of T_{min} and T_{max} and their spatial variability over
 543 North Africa are well correlated to observed values (the mean correlation coefficient over
 544 the 222 SYNOP ground-stations included in the considered domain is around 0.75 for T_{min}
 545 and T_{max}). The annual averaged bias over these stations remains also small, $-0.06^{\circ}C$ for
 546 T_{min} and $-0.4^{\circ}C$ for T_{max} . Note that, at smaller-scale, biases nevertheless become larger. For
 547 instance, in the Sahelian belt during the heatwave, T_{min} is underestimated (up to $2.5^{\circ}C$) at
 548 some ground-stations.

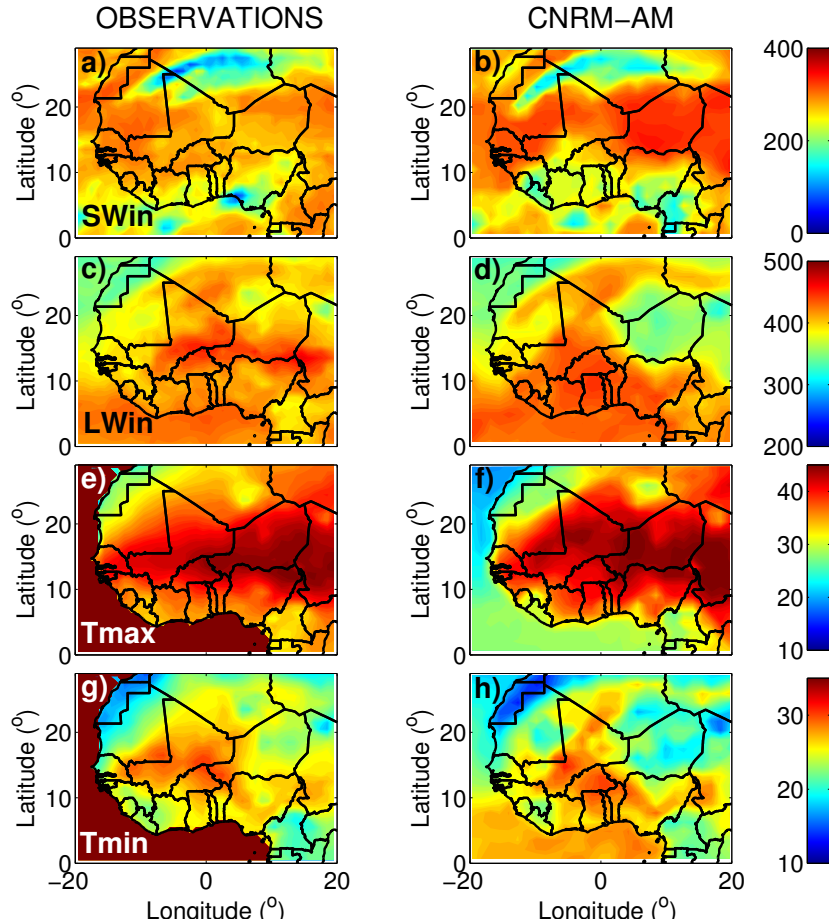


Fig. 7 Incoming shortwave flux SW_{in} (a,b) and longwave flux LW_{in} (c,d) at the surface in W/m^2 ; T_{max} (e,f) and T_{min} (g,h) in $^{\circ}C$ over North Africa given by CERES or BEST observations (left) and CNRM-AM simulation (right) on 15 April 2010, ie day 105. Note that there is no data in ocean on panels e and g.

549 In line with the results of Sane et al. [2012]; Hourdin et al. [2015]; Diallo et al. [2017]
 550 which also constrained the atmospheric dynamics of their GCM simulations by a high-
 551 frequency nudging of the wind towards meteorological reanalyses, our CNRM-AM nudged
 552 simulation is also able to capture the main observed spatial patterns at a daily time scale. A
 553 typical comparison between the observed and simulated daily-mean SW_{in} and LW_{in} fluxes,
 554 T_{max} and T_{min} temperatures is shown in Figure 7, for 15 April 2010 (same day as Figure 4).

555 The main features of the incoming fluxes and radiative effects of clouds (dominantly
 556 present in Northern Sahara, Figure 7) are well-captured by CNRM-AM (Figure 7a,b,c,d),
 557 especially in terms of spatial patterns. Similarly, T_{max} patterns are well reproduced, with the
 558 hottest areas located in the Sahel and southern Sahara and the colder area near the west-
 559 ern Saharan coast (Figure 7e,f). The strong T_{min} values are also reasonably simulated, both
 560 over Mali and the northern Sahara, consistently with the realistic simulation of the strong
 561 nighttime LW_{in} (partly due to the high-level clouds present that day, Figure 4a).

562 However, some biases can be noticed, mainly located in Niger and Chad, where SW_{in} is
 563 overestimated and LW_{in} underestimated. These biases could be related to AOD differences.
 564 Indeed, CNRM-AM uses a climatological monthly-mean AOD, whereas AOD on that day
 565 (15 April 2010) exhibits a strong anomaly over these areas (Figure 4b). As a consequence,
 566 the strong observed longwave and shortwave ARE are most likely missed by the model on
 567 this day, which leads to overestimated T_{max} and underestimated T_{min} over Niger and Chad
 568 (Figure 7f,h).

569 5.2 Fluctuations of temperature, humidity and fluxes in the Sahel during the heatwave:
 570 comparison with in-situ data

571 A comparison between simulated and observed time series of temperature, specific humid-
 572 ity and radiative fluxes is presented in Figure 8, at Agoufou, Mali (see location in Figure
 573 1b), within the Sahelian area significantly affected by the heatwave (Figure 3). Here, we
 574 used the simulated fields at the closest grid point to the observational site ($15^{\circ}20'40''N$ and
 575 $1^{\circ}28'45''W$).

576 Before DOY 103, Agoufou is located north of the ITD, the low-atmospheric layers are
 577 dry ($q_v < 3g/kg$) and the surface air temperature is high during daytime ($> 40^{\circ}C$) but sharply
 578 drops at night, down to $23^{\circ}C$. (Figure 8a). SW_{in} is strong during daytime while LW_{in} (and
 579 LW_{net}) decreases to relatively low values during nighttime (Figure 8b,d,e). The Diurnal Tem-
 580 perature Range (DTR) is large, around $20^{\circ}C$ before DOY 103.

581 In-situ observations at Agoufou in 2010 illustrate the impact of the arrival of the mon-
 582 soon flow in the Sahelian belt (this flow migrates northward during springtime, [Couvreur
 583 et al., 2010]): its first incursion occurs on DOY 103. Once the flow has reached the site,
 584 atmospheric water vapor increases, and simultaneously, nighttime temperatures, LW_{in} and
 585 LW_{net} increases ($T_{min} > 30^{\circ}C$). The following 12 days match the local heatwave period, dur-
 586 ing which daytime SW_{in} is reduced and displays a much stronger day-to-day variability due
 587 to the cloud cover. It leads to much lower T_{max} and DTR during cloudy days. During clear-
 588 sky days, DTR is significantly reduced compared to the pre-heatwave period while T_{max}
 589 remains close to its pre-heatwave values ($40-45^{\circ}C$). The daily-average temperature increase
 590 is dominantly driven by that of T_{min} during this heatwave, whereas T_{max} is only weakly
 591 affected by the change of environmental air masses.

592 The incursions of the monsoon flow, as seen by the increase of 2-m specific humidity
 593 are correctly reproduced by CNRM-AM (dotted lines in Figure 8a). The dynamical nudging
 594 thus allows to well constrain the location of the ITD, at least around Agoufou. Consistently,
 595 the increase of T_{min} concomitant with this moistening is also realistically captured, with
 596 T_{min} increasing by about $10^{\circ}C$ between the pre-heatwave and the heatwave periods. The
 597 simulated diurnal fluctuations of radiative fluxes, specific humidity and temperatures are
 598 also close to observations, despite some biases, most likely due to the representation of
 599 clouds and can be summarized as follows:

- 600 1. Day-to-day variability of SW_{in} is underestimated during the heatwave period (especially
 601 during the cloudy period from day 107 to 112, Figure 8b). Since shortwave CRE seems
 602 reasonably well reproduced with CNRM-AM (not shown), this overestimation of SW_{in}
 603 points towards either an underestimation of the cloud cover at this site, or an incorrect
 604 phasing in the diurnal cycle of cloud cover.
- 605 2. Consistently, the DTR is overestimated during the heatwaves cloudy days.

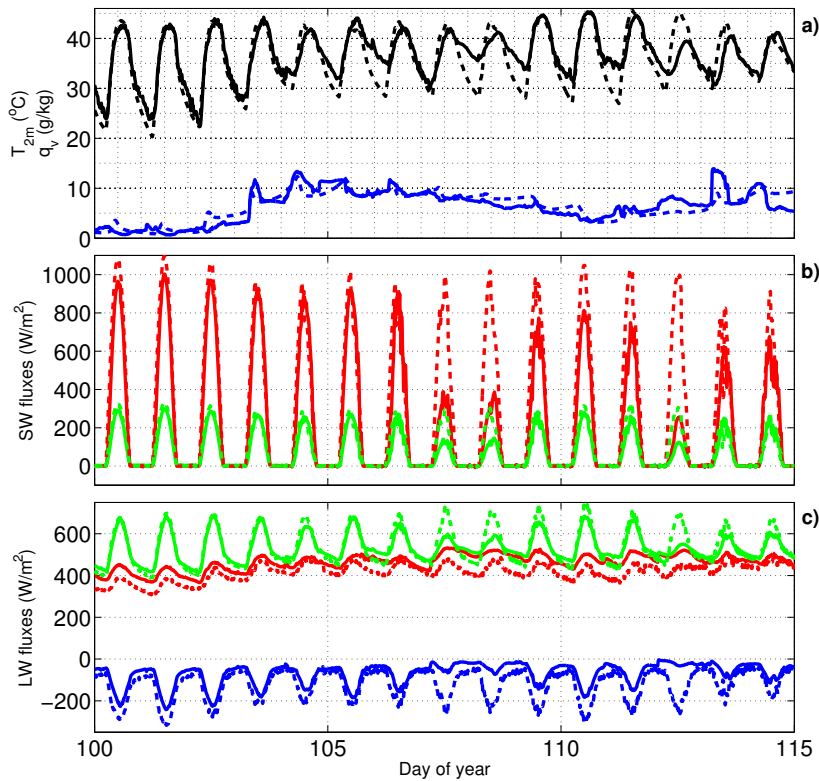


Fig. 8 Time series of: a) 2-m air temperature (black) and specific humidity (blue); b) SW_{in} (red) and SW_{up} (green); c) LW_{in} (red), LW_{up} (green) and LW_{net} (blue) at Agoufou during the heatwave. Solid lines: Local ground observations. Dotted lines: CNRM-AM simulation.

606 3. Finally, LW_{in} is underestimated throughout the diurnal cycle, while LW_{up} is closer to
 607 observations, except for cloudy days for which the simulated SW_{in} leads to an overesti-
 608 mation of the land surface temperature and LW_{up} . Their combination induces an under-
 609 estimated LW_{net} , more pronounced during cloudy days.

610 Even though it remains difficult to draw firm conclusions regarding the role of cloud
 611 during the heatwave, especially because of the shortcomings resulting from the comparison
 612 between local measurements and a model grid pixel of 1.4° , CNRM-AM is able to cap-
 613 ture part of the major observed characteristics of the T_{min} and LW_{in} evolutions, especially
 614 their synchronous increase when the monsoon flow reaches Agoufou. CNRM-AM can thus
 615 be used to further understand part of the role of water vapor in the T_{min} evolution. Note
 616 however that the increase in T_{min} and LW_{in} are weaker in CNRM-AM, which suggests an
 617 underestimation of the impact of humidity on 2m-temperatures and longwave fluxes. The
 618 SARAWI model will be used in section 6 to further explore this humidity impact.

619 5.3 Physical processes acting at local scale : the impacts of turbulence and longwave
620 radiation

621 In order to investigate the processes at play in the low atmospheric layers, we analyze the
622 daytime and nighttime temperature budgets in the first atmospheric layer of the CNRM-AM
623 simulation. Figure 9 shows the daytime and nighttime variations of temperatures for each
624 day of April 2010 (purple) at gridpoint nearest to Agoufou, together with the contribution
625 of each physical process: boundary-layer turbulence, longwave and shortwave radiation,
626 large-scale precipitation and condensation, parameterized deep and shallow convection, and
627 advection, that correspond to the contributions of the different processes to the thermody-
628 namics equation (here, they are cumulated either over the daytime hours, i.e. from sunrise
629 to sunset, or nighttime hours). The total temperature variation (purple) is the sum of each of
630 the previously listed contributions.

631 The CNRM-AM nocturnal cooling is almost entirely due to longwave radiation (Figure
632 9b), whereas its daytime warming mainly results from the balance between the longwave
633 radiative warming and the turbulent cooling (Figure 9a). Surprisingly, during daytime, the
634 longwave warming dominates the temperature variation at the first atmospheric level and
635 overcompensates the turbulence. The net daytime effect of turbulence is to cool the first
636 atmospheric level. This cooling mainly acts in the afternoon by vertical mixing of the first
637 layer with the colder layers above (more details in section 6.1 and Figure 11). The temper-
638 ature advection only plays a minor role in the evolution of the first air layer temperature.
639 Therefore, the fluctuations of surface air temperature during the heatwave episode are dom-
640 inantly driven by longwave radiative and turbulent processes.

641 Figure 10a,b illustrates the evolution of the nighttime surface energy budget. This night-
642 time budget is dominated by the net radiative cooling $R_{net} = LW_{net}$, and very slightly com-
643 pensated with a weak warming from the surface by the sensible heat flux (Figure 10a).
644 Note that, after DOY 103, when the ITD overpasses Agoufou, the nighttime net cooling
645 R_{net} weakens, compared to the pre-heatwave period. Both LW_{in} and LW_{up} increase, but LW_{in}
646 increases more than LW_{up} , which leads to an increase in LW_{net} and enhances the radi-
647 ative coupling between the surface and the lower troposphere. This further induces a weaker
648 nighttime cooling of the lower atmospheric layer (Figure 9b).

649 5.4 Impact of water vapor on atmospheric longwave emissivity

650 The land surface longwave emissivities ϵ_s can be retrieved from:

$$LW_{up} = \sigma \cdot \epsilon_s \cdot T_s^4 \quad (13)$$

651 We can also estimate an atmospheric “effective” longwave emissivity ϵ_a from LW_{in} and the
652 temperature of the lower layer (e.g. [Prata, 1996] among others), using:

$$LW_{in} = \sigma \cdot \epsilon_a \cdot T_a^4 \quad (14)$$

653 Figure 10c illustrates the April 2010 time series of the nighttime values of ϵ_s (red) and ϵ_a
654 (black), computed from CNRM-AM fields. The evolution of this air longwave emissivity ϵ_a
655 at Agoufou is strongly correlated ($r = 0.94$) with the nighttime average 2m specific humidity
656 (Figure 10c,d). Note that this correlation still holds at smaller time-scales (not shown). It
657 illustrates the increase of longwave emissivity associated with an increase of the amount of
658 water vapor. The time series of ϵ_a is well-approximated by the linear regression using 2m

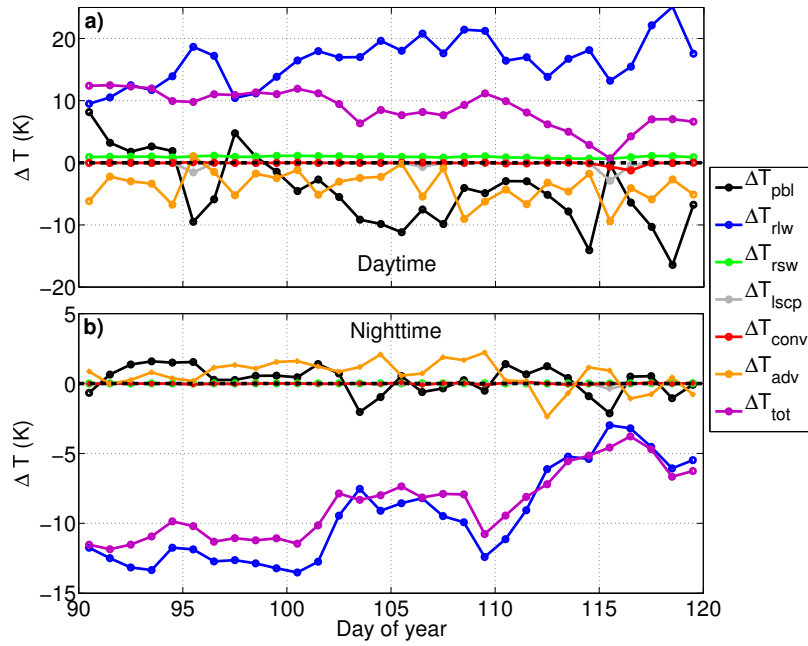


Fig. 9 Time series of daytime (a) and nighttime (b) ΔT temperature variation at the first atmospheric level (purple) and the corresponding contribution of each physical parameterization during April 2010 at Agoufou, in CNRM-AM simulation. Black: planetary boundary layer (pbl); blue: radiative longwave (rlw); green: radiative shortwave (rsw); grey: large-scale condensation and precipitation (lscp); red: deep and shallow convection (conv); orange: advection (adv).

659 specific humidity and 2m air temperature presented in equation 9 (with values of a_i fitted at
 660 Agoufou, blue curve in Figure 10c).

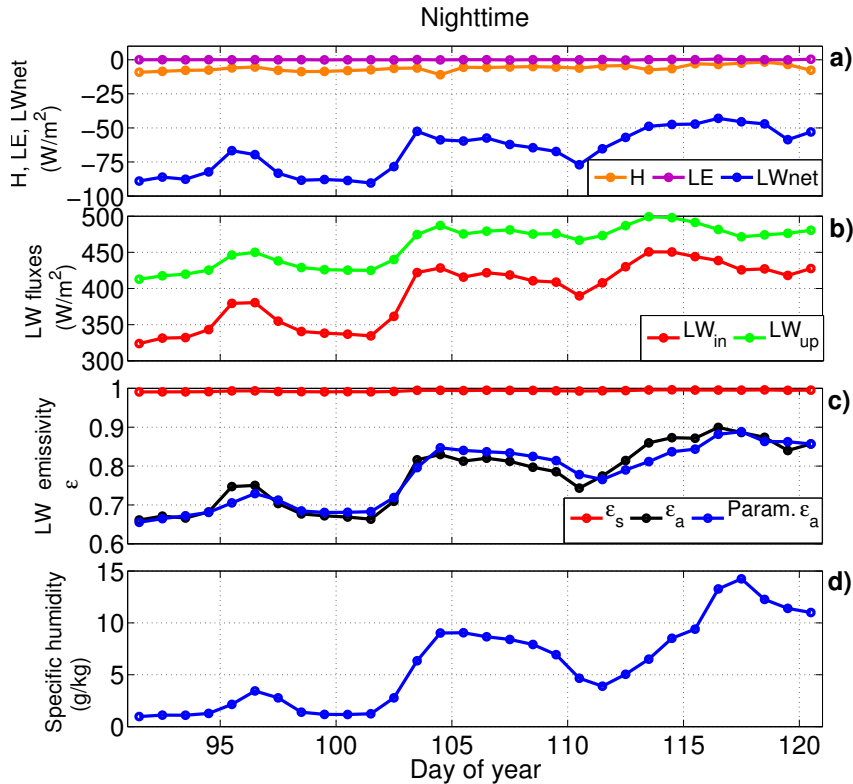


Fig. 10 Time series of nighttime surface fluxes H , LE and LW_{net} (a), LW_{in} and LW_{up} (b), ϵ_s , ϵ_a and parameterized ϵ_a , cf section 5.4 (c), and 2m specific humidity (d) in April 2010 at Agoufou, in the CNRM-AM simulation.

661 **6 Insights from a conceptual prognostic model : quantification of a Humidity** 662 **Radiative Effect (HRE)**

663 Here, the SARAWI model presented in section 2.5 is used to investigate further the impact
664 of water vapor. To this end, we introduce a Humidity Radiative Effect (HRE, detailed in sub-
665 section 6.3). SARAWI explicitly parameterizes the effect of water vapor on the air longwave
666 emissivity (equation 9).

667 This model assumes that synoptic and regional scale motions associated with the mon-
668 soon flow and the tropical plume can be decoupled from physical processes operating at
669 local scale, and therefore the CNRM-AM wind and specific humidity fields are used as in-
670 puts to the SARAWI model. Then, the model directly solves the effects of turbulence and
671 radiative transfer between the soil and the atmospheric surface layer, as these two processes
672 have been identified as the major drivers of the temperature fluctuations (section 5).

673 Simulations are performed with SARAWI over April 2010, either in 1D at the site of
674 Agoufou, and in 3D over North Africa.

In the following, we first evaluate the time evolution of the SARAWI variables given in equations (1) to (8) with the help of the CNRM-AM simulations (section 6.1) before evaluating the 3D SARAWI computation over North Africa (section 6.2). Then, another simulation is made with a constant specific humidity field to evaluate an HRE at Agoufou during the heatwave (section 6.3), and over North Africa (section 6.4). Finally, we demonstrate that the observed anomaly of LW_{in} in North Africa can be explained by means of the HRE quantified with SARAWI (section 6.5).

6.1 Evaluation of the representation of turbulence and longwave radiation

Figure 11 presents a comparison of the time evolution of $\frac{\partial T_a}{\partial t}_{rlw}$, $\frac{\partial T_a}{\partial t}_{pbl}$, LW_{net} and H simulated by CNRM-AM and SARAWI at Agoufou, zoomed over a 5-day window during the heatwave period. This period is centered around DOY 103, which corresponds to the first incursion of the monsoon flow at the site. It is chosen to point out the evolution of the diurnal cycles during the transition from the pre-heatwave towards the heatwave period, but a similar good match between SARAWI and CNRM-AM outputs is found throughout April 2010 (see Figure 13 detailed in the following sections).

Indeed, SARAWI faithfully replicates the diurnal fluctuations simulated by CNRM-AM, for the four parameterized fluxes and temperature tendencies. Similarly, time series of T_s , T_{2m} and T_a given by SARAWI are very close to those computed by CNRM-AM (Figure 11e,f), with only minor deviations (the mean biases over April 2010 are $0.15^\circ C$, $0.5^\circ C$ and $0.9^\circ C$ respectively for T_a , T_{2m} and T_s , with $r > 0.98$ for all three temperatures).

SARAWI also reproduces quite well the transition between the pre-heatwave regime (higher DTR, stronger nighttime air radiative cooling, lower daily-mean LW_{net}) and the heatwave regime (lower DTR, lower nighttime air radiative cooling, higher LW_{net}). This ability of SARAWI to reproduce this transition points out the crucial impact of atmospheric water vapor on longwave air emissivity, and thus on the increase of temperature and fluxes. From these results, the following scenario, which implies a water vapor greenhouse effect, can be formulated:

1. The increase of specific humidity associated with the monsoon flow increases ϵ_a , that in turn increases LW_{in} .
2. This increase of LW_{in} increases the radiative warming of the soil surface layer, and thus also T_s (Figure 11e)
3. Synchronously, the increase of T_s leads to an increase of LW_{up} .
4. LW_{in} however increases more than LW_{up} , which leads to an increase of LW_{net} (Figure 11c).
5. The increase of LW_{in} corresponds to a loss of energy for the air layer, but this loss is more than compensated by an increased infrared absorption of LW_{up} in this layer. Indeed, the latter is enhanced by both higher LW_{up} and air absorptivity (equal to ϵ_a); whereas the former is solely increased by higher ϵ_a .
6. This finally results in less nighttime radiative cooling of the air layer and therefore in a higher T_a in the heatwave period than before.

This water vapor greenhouse effect involves a positive feedback: higher LW_{in} leads to a warmer surface, which in turns leads to a warmer air layer, and therefore higher LW_{in} . The magnitude of this feedback is limited as higher LW_{in} also means a loss of energy of the air layer, which negatively feeds back on T_a . The resulting heatwave equilibrium involves a

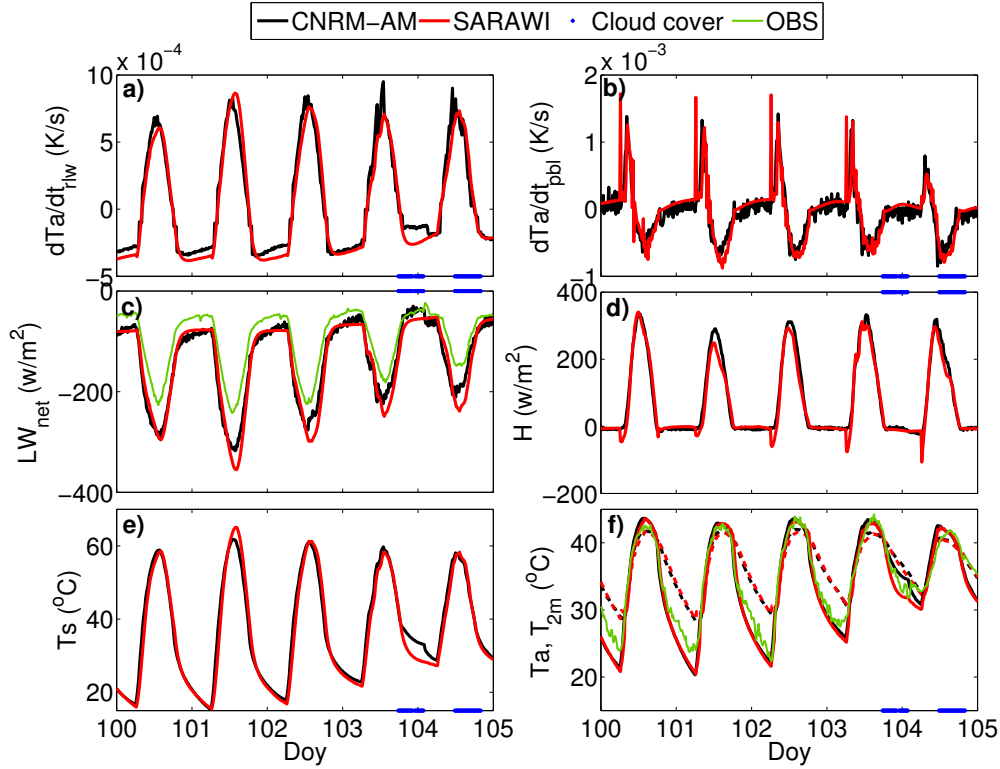


Fig. 11 Time series of $\frac{\partial T_a}{\partial t_{rlw}}$ (a), $\frac{\partial T_a}{\partial t_{pbl}}$ (b), LW_{net} (c), H (d), T_s (e) and T_a (f, dotted lines) and T_{2m} (f, solid lines) for 5 days of the heatwave at Agoufou, in SARAWI (red) and CNRM-AM simulation (black). Blue dots at the top or bottom of panels indicate the presence of clouds in CNRM-AM. Observed LW_{net} and T_{2m} are superimposed in green in panels (c) and (f) respectively.

719 balance between these two feedbacks, which happens on a very short timescale, during the
720 first heatwave night.

721 SARAWI exhibits few departures from CNRM-AM, mainly during the night of DOY
722 104, due to the presence of clouds in the CNRM-AM simulation (cf blue dots in Figure 11).
723 Cloud longwave radiative effects are not represented in the SARAWI model, and that night,
724 the presence of clouds is associated with enhanced LW_{in} in CNRM-AM, which leads to
725 higher T_s and T_{2m} than in SARAWI (the differences reaches up to $3^\circ C$). Interestingly, these
726 SARAWI biases provide inferences on the longwave CRE both on fluxes and temperatures.

727 Finally, the available observations at Agoufou are superimposed in blue in Figure 11.
728 The observed LW_{net} is underestimated by both CNRM-AM and SARAWI due to an under-
729 estimation of LW_{in} , throughout the diurnal cycle, as discussed in section 5.2. Nevertheless,
730 the observed T_{2m} is quite well reproduced with CNRM-AM and SARAWI, except towards
731 the end of the night. This can be explained as follows: the daytime underestimation on LW_{net}
732 has a low impact of T_{2m} since shortwave fluxes are significantly stronger so that the daytime
733 energy budget is dominated by shortwave which is correctly reproduced with these models.
734 However, the nighttime underestimation of LW_{net} leads to a stronger cooling and therefore to

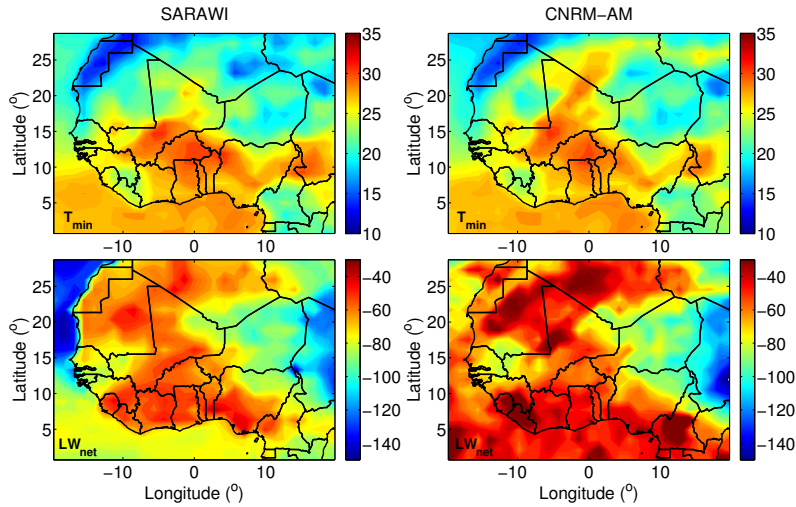


Fig. 12 T_{min} (a,b) and LW_{net} (c,d) fields given by SARAWI (left) and CNRM-AM (right) on 15 April 2010, ie doyr 105.

735 a slightly underestimated end-of-night T_{2m} . Note that the underestimation of LW_{in} is due to
 736 an underestimation of ϵ_a , which could be solved in SARAWI if equation (9) was regressed
 737 with observed data, rather than with CNRM-AM data as done in the current version of the
 738 model.

739 6.2 Maps of T_{min} and longwave fluxes over North Africa

740 SARAWI is further used in a 3D mode over North Africa. The main geographical patterns
 741 of T_{min} and LW_{net} given by CNRM-AM are well reproduced by SARAWI. An example is
 742 shown in Figure 12 for 15 April 2010. Similar results are found for every days of April.

743 The most notable biases are found in the northern Sahara for T_{min} and LW_{net} , which are
 744 most likely related to the neglect of longwave CRE in SARAWI. There, the cloud cover
 745 is high in both observations and CNRM-AM, and induces significant longwave CRE and
 746 nighttime warming (Figures 4 and 7).

747 Apart from those cloud-related impacts, the agreement between CNRM-AM and SARAWI
 748 over the region, both in terms of patterns and orders of magnitude, validates the hypothe-
 749 ses at the heart of the SARAWI model, and underlines the nature of the scale interactions
 750 between large-scale circulations and local physical processes: the dynamics of the monsoon
 751 flow and that of the tropical plume event over the Sahara, drive regional and synoptic-scale
 752 advection of atmospheric water vapor. From there, radiative and turbulent processes, which
 753 act at local and subdiurnal scales, subsequently drive the evolution of the longwave fluxes,
 754 soil and low-level air temperatures.

755 In summary, the high nighttime temperatures observed during the heatwave do not result
 756 from some synoptic advection of warm air masses (since synoptic advection is neglected in
 757 equation (1)). Rather, the synoptic advection of water vapor is the most important component

758 as it increases the low-level air opacity and emissivity (that explicitly depends upon the
 759 specific humidity, which is prescribed in SARAWI, through equation (9)). This results in
 760 an increase of T_{min} , which is dominantly controlled by atmospheric radiative transfer and
 761 boundary-layer turbulence, since they are the only processes parameterized in SARAWI
 762 (equation (1)).

763 6.3 Quantification of the Humidity Radiative Effect (HRE)

764 Figure 13 shows, for April 2010 at Agoufou, time series of LW_{in} (a), T_{2m} (b), T_{max} (c, dashed
 765 lines) and T_{min} (c, solid lines) computed by SARAWI (red), and CNRM-AM (black). The
 766 high correlation between the CNRM-AM and SARAWI time series echoes the results pre-
 767 sented in the previous section. Differences between CNRM-AM and SARAWI only occur
 768 during the most heavily cloudy days (blue dots in Figure 13).

769 An additional 3D simulation is performed with SARAWI where specific humidity re-
 770 mains constant in time; for each grid point, it equals its nighttime average value on 1 April
 771 2010 (hereafter referred to as hus_0). On 1 April 2010, the specific humidity field displays
 772 high values south of the ITD (around $12^\circ N$), within the monsoon flow, and much lower val-
 773 ues north of the ITD. At Agoufou, located north of the ITD on 1 April, the specific humidity
 774 remains low, around $1 g/kg$, which is close to its dry season average. The humidity radiative
 775 effect associated with the increase of ε_a during the heatwave is therefore discarded in this
 776 simulation, whose results are shown in blue in Figure 13.

777 LW_{in} and T_{2m} are very close to their values in the reference simulation until DOY 103.
 778 Afterwards, during the heatwave, the two simulations diverge. In the constant moisture sim-
 779 ulation, little change in the diurnal fluctuations before and after DOY 103 is simulated, at
 780 least until DOY 115 (Figure 13). Overall, daily maxima are close to the reference SARAWI
 781 simulation, but the nighttime characteristics of the heatwave period are not reproduced in
 782 the constant moisture simulation; LW_{in} and T_{min} remain significantly lower, which reveals
 783 the strong sensitivity of the system to the specific humidity.

784 The temperature variation due to the Humidity Radiative Effect is further quantified
 785 with: $\Delta T_{min}^{HRE} = T_{min} - T_{min}^{hus_0}$ where $T_{min}^{hus_0}$ is the value of T_{min} in the constant humidity sim-
 786 ulation. Similarly, we define $\Delta LW_{in}^{HRE} = LW_{in} - LW_{in}^{hus_0}$ for quantifying the HRE on the
 787 incoming longwave flux. At Agoufou, the averaged ΔLW_{in}^{HRE} during the heatwave reaches
 788 $59 W/m^2$, associated with an averaged ΔT_{min}^{HRE} of $4.75^\circ C$, that reaches values higher than
 789 $6.5^\circ C$ between DOY 105 and 109.

790 When compared to the observed estimates of longwave CRE and ARE (Figure 5) which
 791 are respectively of 15 and $19 W/m^2$ on average during the heatwave at Agoufou, the current
 792 estimate emphasizes that HRE stands as the dominant driver of the nighttime warming.
 793 According to those estimations, HRE explains 64% of the total radiative warming during the
 794 heatwave, while ARE explains 20% and CRE 16%, and HRE leads to a nighttime increase
 795 of 2m-temperature up to $6.5^\circ C$, at Agoufou.

796 6.4 Maps of the HRE over North Africa

797 The spatial structure of ΔLW_{in}^{HRE} and ΔT_{HRE} is shown in Figure 14a,b for the 15 April 2010
 798 at 06 UTC, together with the specific humidity field (Figure 14d) and the difference between
 799 specific humidity on 15 April 2010 and the constant specific humidity field prescribed in the

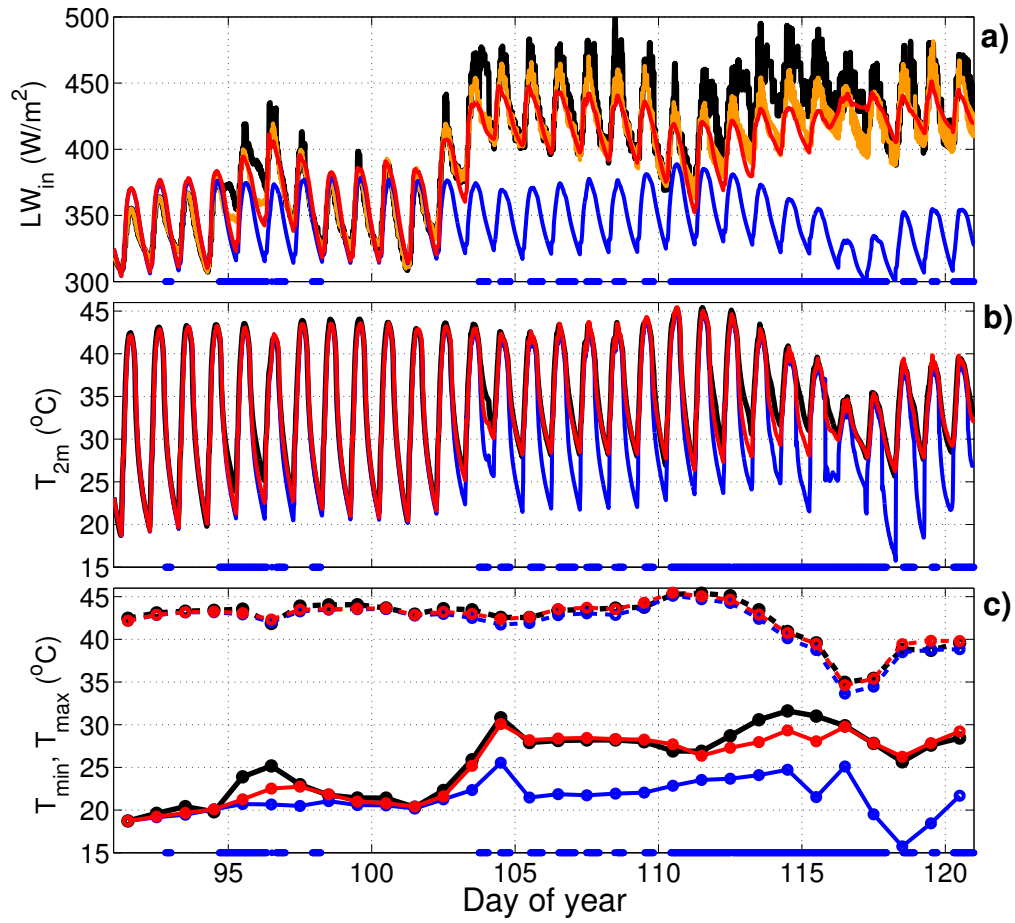


Fig. 13 Time series at Agoufou for April 2010 of: LW_{in} (a), T_{2m} (b), T_{max} (c, dashed lines) and T_{min} (c, full lines). Black: CNRM-AM. Red: SARAWI reference simulation. Blue: SARAWI simulation with constant humidity. Orange: clear-sky LW_{in} computed by CNRM-AM. Blue dots at the bottom of panels: cloud cover in CNRM-AM.

800 constant moisture simulation (Figure 14c). The location of the ITD (here defined as the line
 801 of constant humidity equal to 8g/kg) is indicated with the white line.

802 ΔLW_{in}^{HRE} reaches strong values, up to $100W/m^2$ south of the ITD, leading to ΔT_{HRE}
 803 up to $13^\circ C$. In Figure 14, this strong HRE warming south of the ITD is associated with the
 804 northward progression of the monsoon flow in the previous days, and accounts for a specific
 805 humidity increase of about $10g/kg$ (Figure 14c).

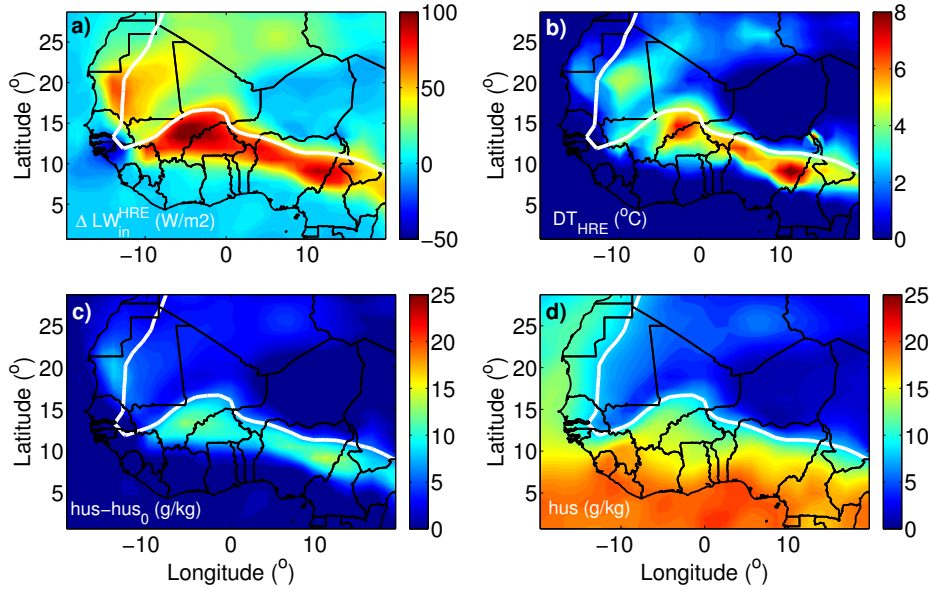


Fig. 14 ΔLW_{in}^{HRE} (a), ΔT_{HRE} (b), $hus - hus_0$ (c), hus (d) given by SARAWI on 15 April 2010, ie doy 105 (see text for definitions). White line: ITD, defined with $hus = 8g/kg$.

806 Over the Sahara and other areas north of the ITD, the high values of ΔLW_{in}^{HRE} and
 807 ΔT_{HRE} are associated with the tropical plume, which also enhances low-level humidity and
 808 reaches about $5^{\circ}C$ (Figure 14c,d).

809 Figure 14 also underlines that the western Sahel (west to $0^{\circ}E$) is more affected by HRE
 810 than the eastern Sahel (east to $0^{\circ}E$), consistently with an ITD that does not reach eastern
 811 Sahel in April 2010 (Figure 14d). The processes affecting the western and eastern Sahel are
 812 therefore distinct, which partly explains why T_{min} were lower in Eastern Sahel (Figure 7).
 813 However, HRE affects Nigeria and areas located to the east of $0^{\circ}E$ but south of $12^{\circ}N$, which
 814 could also partly explains why T_{min} are high in this area (Figure 7g,h).

815 6.5 Can we explain the observed LW_{in} anomalies with the SARAWI HRE estimate ?

816 On average over the Sahel and Sahara, ΔLW_{in}^{HRE} reaches high values. Since HRE is caused
 817 by moisture which is anomalously high in April 2010 over the Sahel and Sahara (Figure
 818 6e,f), here we analyze whether the observed anomalies of LW_{in} that were explained neither
 819 by CRE nor ARE anomalies (section 4) can be better explained by HRE.

820 The HRE longwave anomaly HRE^{ano} is computed by assuming that the LW_{in} climato-
 821 logical anomaly on DOY 91 (1 April 2010) is the sum of the longwave CRE, ARE and HRE
 822 anomalies. Then, we compute $HRE^{ano} = \Delta LW_{in}^{HRE} + HRE_0^{ano}$, with HRE_0^{ano} being the HRE
 823 anomaly on 1 April.

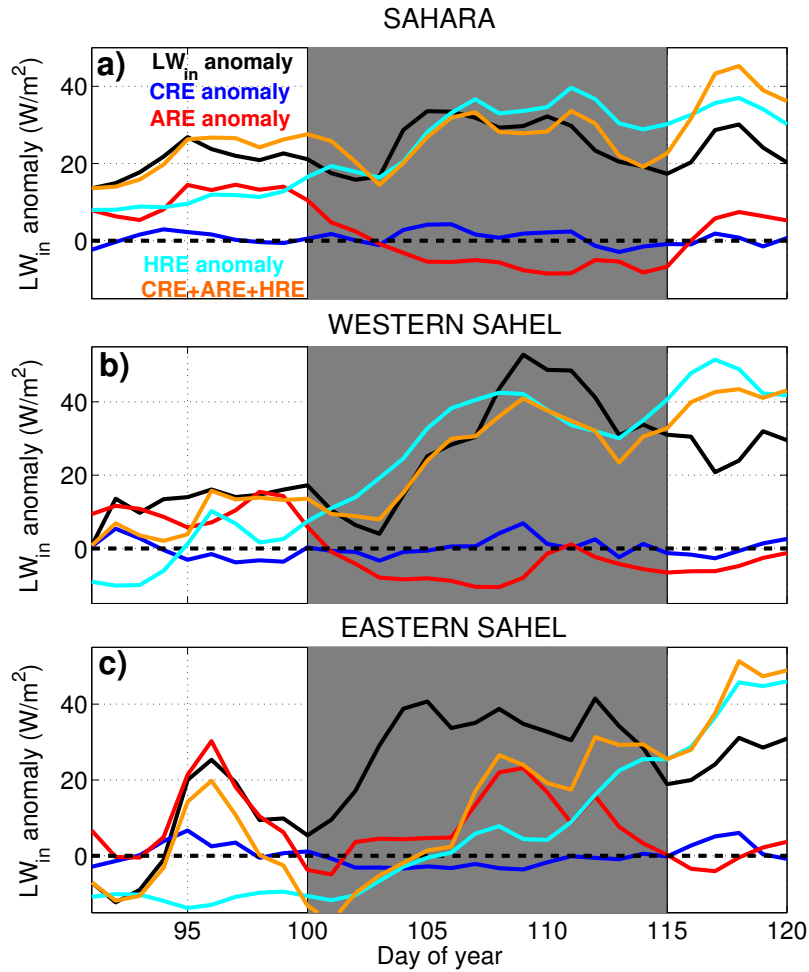


Fig. 15 April 2010 time series of anomalies of: LW_{in} (black), longwave CRE (blue), longwave ARE (red) observed by CERES, longwave HRE computed by SARAWI (light blue) longwave CRE+ARE+HRE (orange); averaged over the Sahara (c), the western Sahel (west to 0° , b), the eastern Sahel (east to 0° , c).

824 Figure 15 shows the April 2010 time series of longwave HRE^{ano} anomalies (light blue),
 825 together with the LW_{in} anomalies (black), longwave CRE (blue) and longwave ARE ana-
 826 malies (red) observed with CERES, as well as the sum of the longwave anomalies CRE+ARE+HRE
 827 (orange), averaged over three areas: the Sahara (a), the western Sahel (b) and the eastern Sa-
 828 hel (c).

829 First, the order of magnitude of HRE^{ano} successfully matches that of the LW_{in} anomalies,
 830 particularly over the Sahara and the western Sahel. Secondly, when SARAWI estimates of
 831 HRE anomalies are added with CRE and ARE anomalies from CERES (orange curves), the

832 resulting time series follows rather closely the observed LW_{in} anomalies (black), over the
833 Sahara and the western Sahel.

834 This result suggests that in the Sahara, the strong positive anomaly of LW_{in} , which was
835 not related to cloud or aerosol anomalies between DOY 100 and 120 is largely explained
836 by the evolution of the HRE induced by the low-level advection of humidity operated by
837 the tropical plume event (Figure 15a). In the western Sahel (Figure 15b), this HRE also
838 explains a major part of the observed anomaly, and is related to a northward penetration of
839 the monsoon flow.

840 In the eastern Sahel, which is more affected by aerosols due to a strong dust episode after
841 DOY 105, HRE remains weaker before DOY 105 (Figure 15c). It increases later, when the
842 ITD migrates northward in the eastern Sahel, and can explain the increase of LW_{in} anomalies
843 in late April. However, in this area, the high anomaly of LW_{in} between DOY 100 and 107
844 is neither explained by clouds or aerosols nor by humidity radiative effects, which suggests
845 the possible influence of other physical processes (complex radiative interactions that arise
846 from overlapping between different types of aerosols and clouds; radiative influence of other
847 greenhouse gases,...). In addition, the low number of in-situ observations assimilated in the
848 reanalysis over Eastern Sahel may also play some role.

849 7 Discussion and conclusion

850 North Africa experienced a major heatwave in April 2010. The present study investigated
851 physical processes acting during this event, using high frequency ground data (AMMA-
852 CATCH), long-term gridded daily temperatures (BEST), satellite-based observations (CERES),
853 climate model simulations (CNRM-AM), and a new soil-surface air layer prognostic model
854 (SARAWI).

855 During spring 2010, very high daily minimum and maximum temperatures were ob-
856 served North of 14°N, over large parts of the Sahel and Sahara, together with strong positive
857 anomalies of LW_{in} and negative anomalies of SW_{in} at the surface, as well as strong positive
858 anomalies of AOD, cloud cover and PW. The cloud cover and PW anomalies are associ-
859 ated with two distinct synoptic events (a tropical plume that reached the northern Sahara
860 and a northward penetration of the monsoon flow in western Sahel), while the strong AOD
861 anomaly that prevails during this period is centered on central Sahel.

862 The heatwave (identified with the methodology of Barbier et al. [2018]) lasts from 10
863 to 25 April 2010 and is particularly severe at night. Strong positive correlations are found
864 between PW, T_{min} and LW_{in} , both in space and time, in the areas affected by the heatwave.

865 Satellite estimates show that, during the heatwave, Aerosol Radiative Effects (ARE) is
866 stronger than Cloud Radiative Effects (CRE) by about $+30W/m^2$ for SW_{in} , and $+15W/m^2$
867 for LW_{in} over both the Sahel and the Sahara. The strong negative anomaly of SW_{in} is almost
868 entirely explained by CRE over the Sahara, while it involves a combination of both CRE and
869 ARE, over the Sahel. In contrast, the strong positive anomaly of LW_{in} (about $+30W/m^2$ over
870 both the Sahara and Sahel) is much higher than longwave CRE or ARE anomalies, which
871 means that neither the cloud cover nor the AOD can explain the observed anomalies of
872 incoming longwave fluxes. The strong correlation between observed LW_{in} and PW anomalies
873 points to the significance of a Humidity Radiative Effect (HRE), and this question is further
874 explored with a climate model and a conceptual soil-atmospheric surface layer model.

875 In order to capture the chronology of the heatwave (and thus helps in performing rele-
876 vant quantitative comparisons with observations, down to sub-daily time scales [Diallo et al.,
877 2017]), the dynamics of the climate-model simulation is nudged towards the ERA-interim

878 meteorological reanalysis. We show that the CNRM-AM simulation faithfully reproduces
879 the Saharan tropical plume event and the Sahelian monsoon surge, as well as the spatial pat-
880 terns of surface incoming fluxes and temperatures observed during the heatwave. It exhibits
881 systematic biases though, such as too low LW_{in} , LW_{net} and T_{min} . Those shortcomings do not
882 affect the ability of the model to represent the sharp transition between the pre-heatwave
883 and heatwave regime, closely associated with the arrival of the monsoon flow in the Sahel,
884 whose main observed characteristics are well-reproduced. The pre-heatwave regime is dry
885 with low nighttime temperatures, low LW_{in} and LW_{net} fluxes, and high Diurnal Temperature
886 Range (DTR); while the heatwave regime is moister with higher nighttime temperatures,
887 stronger LW_{in} and weaker DTR, both in observations and simulations.

888 In the CNRM-AM simulation, the nocturnal cooling of the atmospheric surface layer is
889 almost entirely due to longwave radiative transfer, whereas daytime evolution of the surface-
890 layer air temperature results mainly from the combination of two dominant processes: long-
891 wave radiation and turbulence. During the heatwave, nighttime air cooling by longwave ra-
892 diation is lower. Similarly, the nighttime soil cooling is lower, because LW_{in} increases more
893 than LW_{up} . The combination results in a stronger thermal coupling between the soil and the
894 atmospheric surface layer. The increase of LW_{in} is strongly correlated with the increase in
895 humidity on areas where the monsoon flow (Western Sahel) or the tropical plume (Sahara)
896 moistens the environment.

897 The new conceptual model SARAWI (cf section 2.5) is used to explore further the radi-
898 ative greenhouse effect of water vapor. We show that, at first order, regional-scale processes
899 can be decoupled from local physics, namely turbulence and longwave radiative transfer be-
900 tween the soil and the atmospheric surface layer. By prescribing the former (here from the
901 CNRM-AM simulation) and explicitly and pronostically computing the impact of the latter
902 on temperatures, we are able to reproduce with a very good accuracy the surface energy
903 budget, the radiative and turbulent warming of the atmospheric surface layer, LW_{in} fluxes,
904 soil and air temperatures, and their diurnal cycles given by CNRM-AM. Unlike a complex
905 3D GCM, SARAWI is well-suited to perform and interpret sensitivity tests in simple and
906 unambiguous ways. In the present study, it allows us to highlight the crucial impact of water
907 vapor during the heatwave. Over the Sahel, the greenhouse effect of water vapor enhances
908 LW_{in} and T_{min} up to $100W/m^2$ and $13^{\circ}C$ respectively.

909 In addition, a quantitative analysis shows that the sum of the HRE anomaly estimated
910 using SARAWI, with the weaker CRE and ARE anomalies from CERES, explain the evolu-
911 tion of the observed LW_{in} anomaly over the Sahara and the western Sahel. This demonstrates
912 that the increase of air emissivity due to the increase of moisture is the dominant driver of
913 the heatwave nighttime temperatures; and that the severity of this heatwave can be explained
914 by the increased greenhouse effect of water vapor.

915 In summary, our study provides insights into the interactions arising between processes
916 operating at different scales: during the April 2010 heatwave, the synoptic-scale advection
917 of warm air is negligible. However, the synoptic-scale advection of water vapor (associated
918 with either the monsoon flow or the tropical plume) emerges as a fundamental driver. In-
919 deed, the evolution of surface fluxes, soil and surface air temperatures are almost entirely
920 explained by physical processes, among which longwave radiative transfers, which are very
921 sensitive to water vapor variations.

922 Beyond this particular case study, a simplified model such as SARAWI can be useful for
923 carrying sensitivity experiments at very low computation cost; e.g. for the implementation
924 of new physical parameterizations. More broadly, such a modeling approach could also be
925 useful for comparing the physical mechanisms operating in different climate models. This

926 may be particularly relevant here given the importance of physical processes involved in
 927 land-atmosphere interactions on the climate during this period of the year.

928 Finally, this study further raises several open questions:

- 929 – Physical processes and mechanisms driving nighttime temperatures have been high-
 930 lighted, but the evolution of T_{max} during this heatwave appeared complex, and seems
 931 to imply a balance between physical processes. To what extent do cloud, aerosol or hu-
 932 midity shortwave radiative effects lowers T_{max} ? To what extent can a heat accumulation
 933 phenomenon in the upper boundary-layer as described by Miralles et al. [2014] warm
 934 the low-layers during daytime via the afternoon convective and turbulent mixing?
- 935 – Could other processes involving larger-scale circulations, as recently highlighted in mid-
 936 latitudes by Zschenderlein et al. [2019] play a role? In particular for the Sahel, to what
 937 extend and how are tropical waves influencing Sahelian heatwave occurrence and char-
 938 acteristics? At relatively smaller scale, are convectively generated cold pools (which
 939 can advect water vapor up to the Sahara, [Garcia-Carreras et al., 2013]) playing a role
 940 during spring sahelian heatwaves?
- 941 – Barbier et al. [2018] show that there is a strong climatologic nighttime warming trend
 942 during heatwaves. To what extent can this trend be related to a climatic increase of at-
 943 mospheric water vapor content [IPCC, 2013], especially over the Saharan region [Evan
 944 et al., 2015]? And how would this affect wet-bulb temperature which stands as an im-
 945 portant variable with respect to heath considerations (e.g. [Sherwood and Huber, 2010])?
- 946 – Finally, can this link between water vapor and T_{min} help to analyze climate projections
 947 and reduce uncertainties on extreme weather frequency and severity for the coming cen-
 948 tury?

949 A Appendix : Configuration of the SARAWI simulations and tuned coefficients

950 In the SARAWI simulations used in the present study, physiographic and physical parameters are statistically
 951 tuned using the monthly-average values resolved by CNRM-AM. We also differentiate nighttime and daytime
 952 conditions when the considered parameter physically depends on static stability. This leads to:

953 ϵ_a : Coefficients a_i of equation 9 are estimated using longwave fluxes simulated by CNRM-AM which are
 954 regressed with the atmospheric specific humidity and air temperature. We can consider a_i coefficients ob-
 955 tained from a regression that include all points in North Africa, or alternatively use a_i coefficients which vary
 956 depending on the climate zone (Sahara, Sahel, Guinea). Both approaches lead to similar results (with a 5.3
 957 W/m^2 or 1.3% uncertainty on LW_{in} and a $0.28^\circ C$ uncertainty on T_{2m}). A regional fitting over North Africa
 958 gives $a_1 = 0.667$, $a_2 = 1.17 \cdot 10^{-2}$ with hus in g/kg and $a_3 = 4.55 \cdot 10^{-4}$ with T_a in $^\circ C$.

959 ϵ_s : As for ϵ_a , we use CNRM-AM longwave fluxes to estimate ϵ_s (which uses the ECOCLIMAP database,
 960 [Champeaux et al., 2005; Faroux et al., 2013]). It is almost constant and equal to 0.9946 ± 0.0065 over all
 961 North Africa in CNRM-AM. We take this mean-value as a constant for all continental grid points (this leads
 962 to a $0.11 W/m^2$ or 0.03% uncertainty on LW_{in} and a $0.08^\circ C$ uncertainty on T_{2m} as compared to the local value
 963 for each grid point).

964 C_s : In order to correctly fit C_s , we use equation (2) with the resolved fluxes and temperatures given by
 965 CNRM-AM, which takes its soil physiographic characteristics from the ECOCLIMAP database [Champeaux
 966 et al., 2005; Faroux et al., 2013]. We average the different terms for each grid point separately over daytime
 967 and nighttime, from which we estimate two physiographic 2D fields $C_s^{night}(lon, lat)$ and $C_s^{day}(lon, lat)$.

968 h_{rad} : We compute $h_{rad} = c_{rad} \cdot \delta z$ at each grid point by determining the value of h_{rad} that minimizes the
 969 root mean square error between the CNRM-AM values of $\frac{\partial T_a}{\partial t}_{rlw}$ and the estimated values of that tendency
 970 according to equation (6). Results show that the value of c_{rad} is very homogeneous over all continental North
 971 Africa, so we choose to keep one constant value in SARAWI equal to the average over the continental area :
 972 $h_{rad} = 4.74 \cdot \delta z$. Physically, h_{rad} corresponds to a characteristic penetration depth of the upwelling longwave
 973 flux emitted by the surface, or alternatively to the depth of the layer radiatively warmed (or cooled) by the
 974 surface.

975 h_{urb} : It is fixed equal to the height between the first and the second layers of the CNRM-AM simulation
 976 (35m).

977 c_{l2m} : The parameterization available in CNRM-AM [Mahfouf et al., 1995] is used here to prescribe c_{l2m} , in
 978 order to facilitate comparison with the diagnosed T_{2m} in CNRM-AM simulation.

979 C_h , K_s , K_h : In coupled soil-atmospheric models, the drag coefficient C_h usually depends on the static
 980 stability (see Noilhan and Mahfouf [1996] for the ISBA model used in CNRM-AM). Similarly, the turbulent
 981 diffusivity in low-layers also strongly varies with the static stability (e.g. [Yasuda, 1988; Largeron et al.,
 982 2010]).

983 Here, we choose to use constant daytime values: $C_h = 4.10^{-3}$, $K_s = 1.6.10^{-4}$, $K_h = 0.94 \text{ m}^2 \cdot \text{s}^{-1}$; and
 984 constant nighttime values about 8 times lower: $C_h = 5.10^{-4}$, $K_s = 2.10^{-5}$, $K_h = 0.08 \text{ m}^2 \cdot \text{s}^{-1}$. Values are
 985 tuned to recover the heat fluxes given by the CNRM-AM simulation.

986 **Acknowledgements** This work has been done in the framework of the ACASIS project from the French
 987 national research agency (ANR). The authors acknowledge support from ANR ACASIS, grant ANR-13-
 988 487 SENV-0007. Authors also acknowledge NASA for the dissemination of the CERES satellite products
 989 through the website <https://ceres.larc.nasa.gov/>, the Berkeley Earth for their open global temperature database
 990 (berkeleyearth.org/), and the scientists and technicians who collected the AMMA-CATCH data in the Sahel.
 991 They also thank Mireille Tomasini for usefull discussions on heat budget analysis, and Clara Theeten for her
 992 careful proofreadings of the present paper.

993 References

- 994 Balkanski, Y., Schulz, M., Claquin, T., and Guibert, S. (2007). Reevaluation of mineral aerosol radiative
 995 forcings suggests a better agreement with satellite and aeronet data. *Atmospheric Chemistry and Physics*,
 996 7(1):81–95.
- 997 Barbier, J., Guichard, F., Bouniol, D., Couvreur, F., and Roehrig, R. (2018). Detection of intraseasonal large-
 998 scale heat waves: Characteristics and historical trends during the sahelian spring. *Journal of Climate*,
 999 31(1):61–80.
- 1000 Basart, S., Pérez García-Pando, C., Cuevas, E., Baldasano Recio, J. M., and Gobbi, P. (2009). Aerosol
 1001 characterization in northern africa, northeastern atlantic, mediterranean basin and middle east from direct-
 1002 sun aeronet observations. *Atmospheric Chemistry and Physics*, 9(21):8265–8282.
- 1003 Baup, F., Mougín, E., De Rosnay, P., Timouk, F., and Chênerie, I. (2007). Surface soil moisture estimation
 1004 over the amma sahelian site in mali using envisat/asar data. *Remote Sensing of Environment*, 109(4):473–
 1005 481.
- 1006 Beniston, M. (2004). The 2003 heat wave in europe: A shape of things to come? an analysis based on swiss
 1007 climatological data and model simulations. *Geophysical Research Letters*, 31(2).
- 1008 Black, E., Blackburn, M., Harrison, G., Hoskins, B., and Methven, J. (2004). Factors contributing to the
 1009 summer 2003 european heatwave. *Weather*, 59(8):217–223.
- 1010 Bouniol, D., Couvreur, F., Kamsu-Tamo, P.-H., Leplay, M., Guichard, F., Favot, F., and O’Connor, E. J.
 1011 (2012). Diurnal and seasonal cycles of cloud occurrences, types, and radiative impact over west africa.
 1012 *Journal of Applied Meteorology and Climatology*, 51(3):534–553.
- 1013 Brooks, N. and Legrand, M. (2000). Dust variability over northern africa and rainfall in the sahel. In *Linking
 1014 climate change to land surface change*, pages 1–25. Springer.
- 1015 Champeaux, J., Masson, V., and Chauvin, F. (2005). Ecoclimap: a global database of land surface parameters
 1016 at 1 km resolution. *Meteorological Applications*, 12(1):29–32.

- 1017 Coindreau, O., Hourdin, F., Haeffelin, M., Mathieu, A., and Rio, C. (2007). Assessment of physical param-
1018 eterizations using a global climate model with stretchable grid and nudging. *Monthly weather review*,
1019 135(4):1474–1489.
- 1020 Couvreur, F., Guichard, F., Bock, O., Campistron, B., Lafore, J.-P., and Redelsperger, J.-L. (2010). Syn-
1021 optic variability of the monsoon flux over west africa prior to the onset. *Quarterly Journal of the Royal*
1022 *Meteorological Society*, 136(S1):159–173.
- 1023 Cuxart, J., Bougeault, P., and Redelsperger, J.-L. (2000). A turbulence scheme allowing for mesoscale and
1024 large-eddy simulations. *Quarterly Journal of the Royal Meteorological Society*, 126(562):1–30.
- 1025 Decharme, B., Brun, E., Boone, A., Delire, C., Le Moigne, P., and Morin, S. (2016). Impacts of snow and
1026 organic soils parameterization on northern eurasian soil temperature profiles simulated by the isba land
1027 surface model. *The Cryosphere*, 10(2):853–877.
- 1028 Decharme, B., Martin, E., and Faroux, S. (2013). Reconciling soil thermal and hydrological lower boundary
1029 conditions in land surface models. *Journal of Geophysical Research: Atmospheres*, 118(14):7819–7834.
- 1030 Dee, D., Uppala, S., Simmons, A., Berrisford, P., Poli, P., Kobayashi, S., Andrae, U., Balmaseda, M., Bal-
1031 samo, G., Bauer, P., et al. (2011). The era-interim reanalysis: Configuration and performance of the data
1032 assimilation system. *Quarterly Journal of the royal meteorological society*, 137(656):553–597.
- 1033 Deme, A., Gaye, A. T., and Hourdin, F. (2017). *Climate projections in West Africa: the obvious and the*
1034 *uncertain*. In "Rural societies in the face of climatic and environmental changes in West Africa". Eds. B.
1035 Sultan, R. Lalou R., M. A. Sanni, A. Oumarou and M. A. Soumaré, IRD Editions. AN13: 9782709924245
1036 and 9782709924269.
- 1037 Déqué, M., Dreveton, C., Braun, A., and Cariolle, D. (1994). The arpege/ifs atmosphere model: a contribution
1038 to the french community climate modelling. *Climate Dynamics*, 10(4-5):249–266.
- 1039 Diallo, F. B., Hourdin, F., Rio, C., Traore, A.-K., Mellul, L., Guichard, F., and Kergoat, L. (2017). The
1040 surface energy budget computed at the grid-scale of a climate model challenged by station data in west
1041 africa. *Journal of Advances in Modeling Earth Systems*, 9(7):2710–2738.
- 1042 Doelling, D. R., Loeb, N. G., Keyes, D. F., Nordeen, M. L., Morstad, D., Nguyen, C., Wielicki, B. A., Young,
1043 D. F., and Sun, M. (2013). Geostationary enhanced temporal interpolation for ceres flux products. *Journal*
1044 *of Atmospheric and Oceanic Technology*, 30(6):1072–1090.
- 1045 Evan, A. T., Flamant, C., Lavaysse, C., Kocha, C., and Saci, A. (2015). Water vapor–forced greenhouse
1046 warming over the sahara desert and the recent recovery from the sahelian drought. *Journal of Climate*,
1047 28(1):108–123.
- 1048 Faroux, S., Kaptué Tchuenté, A., Roujean, J.-L., Masson, V., Martin, E., and Moigne, P. L. (2013). Ecoclimap-
1049 ii/europe: a twofold database of ecosystems and surface parameters at 1 km resolution based on satellite
1050 information for use in land surface, meteorological and climate models. *Geoscientific Model Development*,
1051 6(2):563–582.
- 1052 Fischer, E. M. (2014). Climate science: autopsy of two mega-heatwaves. *Nature Geoscience*, 7(5):332–333.
- 1053 Fontaine, B., Janicot, S., and Monerie, P.-A. (2013). Recent changes in air temperature, heat waves occur-
1054 rences, and atmospheric circulation in northern africa. *Journal of Geophysical Research: Atmospheres*,
1055 118(15):8536–8552.
- 1056 Fouquart, Y. and Bonnel, B. (1980). Computations of solar heating of the earth's atmosphere- a new param-
1057 eterization. *Beitraege zur Physik der Atmosphaere*, 53:35–62.
- 1058 Fröhlich, L., Knippertz, P., Fink, A. H., and Hohberger, E. (2013). An objective climatology of tropical
1059 plumes. *Journal of Climate*, 26(14):5044–5060.
- 1060 Fu, Q. and Liou, K. (1992). On the correlated k-distribution method for radiative transfer in nonhomogeneous
1061 atmospheres. *Journal of the Atmospheric Sciences*, 49(22):2139–2156.
- 1062 Garcia-Carreras, L., Marsham, J., Parker, D., Bain, C., Milton, S., Saci, A., Salah-Ferroudj, M., Ouchene, B.,
1063 and Washington, R. (2013). The impact of convective cold pool outflows on model biases in the sahara.
1064 *Geophysical Research Letters*, 40(8):1647–1652.
- 1065 Guérémy, J. (2011). A continuous buoyancy based convection scheme: one-and three-dimensional validation.
1066 *Tellus A*, 63(4):687–706.
- 1067 Guichard, F., Kergoat, L., Hourdin, F., Léauthaud, C., Barbier, J., Mougou, E., and Diarra, B. (2017). *Climate*
1068 *warming observed in the Sahel since 1950*. In "Rural societies in the face of climatic and environmental
1069 changes in West Africa". Ed. B. Sultan, R. Lalou, M. A. Sanni, A. Oumarou, M. A. Soumaré. AN13:
1070 9782709924245 and 9782709924269.
- 1071 Guichard, F., Kergoat, L., Mougou, E., and Hourdin, F. (2012). The annual cycle of temperature in the sahel
1072 and its climatic sensitivity. In *AGU Fall Meeting Abstracts*, volume 1, page 1004.
- 1073 Guichard, F., Kergoat, L., Mougou, E., Timouk, F., Baup, F., Hiernaux, P., and Lavenu, F. (2009). Surface
1074 thermodynamics and radiative budget in the sahelian gourma: seasonal and diurnal cycles. *Journal of*
1075 *Hydrology*, 375(1):161–177.

- 1076 Herrero, J. and Polo, M. (2012). Parameterization of atmospheric longwave emissivity in a mountainous site
1077 for all sky conditions. *Hydrology and Earth System Sciences*, 16(9):3139–3147.
- 1078 Honda, Y., Kondo, M., McGregor, G., Kim, H., Guo, Y.-L., Hijioka, Y., Yoshikawa, M., Oka, K., Takano, S.,
1079 Hales, S., et al. (2014). Heat-related mortality risk model for climate change impact projection. *Environ-*
1080 *mental health and preventive medicine*, 19(1):56–63.
- 1081 Hourdin, F., Gueye, M., Diallo, B., Dufresne, J.-L., Escribano, J., Menut, L., Marticoréna, B., Siour, G., and
1082 Guichard, F. (2015). Parameterization of convective transport in the boundary layer and its impact on
1083 the representation of the diurnal cycle of wind and dust emissions. *Atmospheric Chemistry and Physics*,
1084 15(12):6775–6788.
- 1085 IPCC (2013). *Climate change 2013: the physical science basis: Working Group I contribution to the Fifth*
1086 *assessment report of the Intergovernmental Panel on Climate Change*. Cambridge University Press.
- 1087 IPCC (2014). *Climate Change 2014—Impacts, Adaptation and Vulnerability: Regional Aspects*. Cambridge
1088 University Press.
- 1089 Klose, M., Shao, Y., Karremann, M. K., and Fink, A. H. (2010). Sahel dust zone and synoptic background.
1090 *Geophysical Research Letters*, 37(9).
- 1091 Knippertz, P. and Martin, J. E. (2005). Tropical plumes and extreme precipitation in subtropical and tropical
1092 west africa. *Quarterly Journal of the Royal Meteorological Society*, 131(610):2337–2365.
- 1093 Largeron, Y., Staquet, C., and Chemel, C. (2010). Turbulent mixing in a katabatic wind under stable condi-
1094 tions. *Meteorologische Zeitschrift*, 19(5):467–480.
- 1095 Leroux, S., Bellon, G., Roehrig, R., Caian, M., Klingaman, N. P., Lafore, J.-P., Musat, I., Rio, C., and Tyteca,
1096 S. (2016). Inter-model comparison of subseasonal tropical variability in aquaplanet experiments: Effect of
1097 a warm pool. *Journal of Advances in Modeling Earth Systems*.
- 1098 Lohou, F., Kergoat, L., Guichard, F., Boone, A., Cappelaere, B., Cohard, J.-M., Demarty, J., Galle, S., Grippa,
1099 M., Peugeot, C., et al. (2014). Surface response to rain events throughout the west african monsoon.
1100 *Atmospheric Chemistry and Physics*, 14(8):3883–3898.
- 1101 Lopez, P. (2002). Implementation and validation of a new prognostic large-scale cloud and precipitation
1102 scheme for climate and data-assimilation purposes. *Quarterly Journal of the Royal Meteorological Society*,
1103 128(579):229–257.
- 1104 Mahfouf, J., Manzi, A., Noilhan, J., Giordani, H., and Déqué, M. (1995). The land surface scheme isba
1105 within the météo-france climate model arpege. part i. implementation and preliminary results. *Journal of*
1106 *Climate*, 8(8):2039–2057.
- 1107 Marsham, J. H., Parker, D. J., Todd, M. C., Banks, J. R., Brindley, H. E., Garcia-Carreras, L., Roberts, A. J.,
1108 and Ryder, C. L. (2016). The contrasting roles of water and dust in controlling daily variations in radiative
1109 heating of the summertime saharan heat low. *Atmospheric Chemistry and Physics*, 16(5):3563–3575.
- 1110 Martin, G., Peyrillé, P., Roehrig, R., Rio, C., Caian, M., Bellon, G., Codron, F., Lafore, J.-P., Poan, D., and
1111 Idelkadi, A. (2017). Understanding the west african monsoon from the analysis of diabatic heating
1112 distributions as simulated by climate models. *Journal of Advances in Modeling Earth Systems*, 9(1):239–
1113 270.
- 1114 Masson, V., Champeaux, J.-L., Chauvin, F., Meriguet, C., and Lacaze, R. (2003). A global database of
1115 land surface parameters at 1-km resolution in meteorological and climate models. *Journal of climate*,
1116 16(9):1261–1282.
- 1117 Masson, V., Le Moigne, P., Martin, E., Faroux, S., Alias, A., Alkama, R., Belamari, S., Barbu, A., Boone,
1118 A., Bouyssel, F., et al. (2013). The surfexv7. 2 land and ocean surface platform for coupled or offline
1119 simulation of earth surface variables and fluxes. *Geoscientific Model Development*, 6:929–960.
- 1120 Mellor, G. L. and Yamada, T. (1982). Development of a turbulence closure model for geophysical fluid
1121 problems. *Reviews of Geophysics*, 20(4):851–875.
- 1122 Michou, M., Nabat, P., and Saint-Martin, D. (2015). Development and basic evaluation of a prognostic aerosol
1123 scheme (v1) in the cnrm climate model cnrm-cm6. *Geoscientific Model Development*, 8(3).
- 1124 Miralles, D. G., Teuling, A. J., Van Heerwaarden, C. C., and de Arellano, J. V.-G. (2014). Mega-heatwave
1125 temperatures due to combined soil desiccation and atmospheric heat accumulation. *Nature geoscience*,
1126 7(5):345–349.
- 1127 Mlawer, E. J., Taubman, S. J., Brown, P. D., Iacono, M. J., and Clough, S. A. (1997). Radiative transfer for
1128 inhomogeneous atmospheres: Rrtm, a validated correlated-k model for the longwave. *Journal of Geophys-*
1129 *ical Research: Atmospheres*, 102(D14):16663–16682.
- 1130 Moron, V., Oueslati, B., Pohl, B., Rome, S., and Janicot, S. (2016). Trends of mean temperatures and warm
1131 extremes in northern tropical africa (1961–2014) from observed and ppca-reconstructed time series. *Jour-*
1132 *nal of Geophysical Research: Atmospheres*, 121(10):5298–5319.
- 1133 Mougou, E., Hiernaux, P., Kergoat, L., Grippa, M., De Rosnay, P., Timouk, F., Le Dantec, V., Demarez, V.,
1134 Lavenu, F., Arjounin, M., et al. (2009). The amma-catch gourma observatory site in mali: Relating climatic
1135 variations to changes in vegetation, surface hydrology, fluxes and natural resources. *Journal of Hydrology*,

- 1136 375(1):14–33.
- 1137 Nabat, P., Somot, S., Mallet, M., Chiapello, I., Morcrette, J., Solmon, F., Szopa, S., Dulac, F., Collins, W.,
1138 Ghan, S., et al. (2013). A 4-d climatology (1979–2009) of the monthly tropospheric aerosol optical depth
1139 distribution over the mediterranean region from a comparative evaluation and blending of remote sensing
1140 and model products. *Atmospheric Measurement Techniques*, 6(5):1287.
- 1141 Noilhan, J. and Mahfouf, J.-F. (1996). The isba land surface parameterisation scheme. *Global and planetary*
1142 *Change*, 13(1-4):145–159.
- 1143 Noilhan, J. and Planton, S. (1989). A simple parameterization of land surface processes for meteorological
1144 models. *Monthly Weather Review*, 117(3):536–549.
- 1145 Perkins, S. E. (2015). A review on the scientific understanding of heatwaves—their measurement, driving
1146 mechanisms, and changes at the global scale. *Atmospheric Research*, 164:242–267.
- 1147 Piriou, J.-M., Redelsperger, J.-L., Geleyn, J.-F., Lafore, J.-P., and Guichard, F. (2007). An approach for
1148 convective parameterization with memory: Separating microphysics and transport in grid-scale equations.
1149 *Journal of the Atmospheric Sciences*, 64(11):4127–4139.
- 1150 Prata, A. (1996). A new long-wave formula for estimating downward clear-sky radiation at the surface.
1151 *Quarterly Journal of the Royal Meteorological Society*, 122(533):1127–1151.
- 1152 Ramanathan, V., Cess, R., Harrison, E., Minnis, P., Barkstrom, B., et al. (1989). Cloud-radiative forcing and
1153 climate: Results from the earth radiation budget experiment. *Science*, 243(4887):57.
- 1154 Ricard, J. and Royer, J.-F. (1993). A statistical cloud scheme for use in an agcm. *Annales Geophysicae*,
1155 11:1095–1115.
- 1156 Roehrig, R., Bouniol, D., Guichard, F., Hourdin, F., and Redelsperger, J.-L. (2013). The present and future of
1157 the west african monsoon: a process-oriented assessment of cmip5 simulations along the amma transect.
1158 *Journal of Climate*, 26(17):6471–6505.
- 1159 Rohde, R., Muller, R., Jacobsen, R., Perlmutter, S., Rosenfeld, A., Wurtele, J., Curry, J., Wickhams, C., and
1160 Mosher, S. (2013). Berkeley earth temperature averaging process, geoinfor. geostat.: An overview 1 : 2.
1161 *of*, 13:20–100.
- 1162 Rutan, D. A., Kato, S., Doelling, D. R., Rose, F. G., Nguyen, L. T., Caldwell, T. E., and Loeb, N. G. (2015).
1163 Ceres synoptic product: Methodology and validation of surface radiant flux. *Journal of Atmospheric and*
1164 *Oceanic Technology*, 32(6):1121–1143.
- 1165 Sane, Y., Bonazzola, M., Rio, C., Chambon, P., Fiolleau, T., Musat, I., Hourdin, F., Roca, R., Grandpeix,
1166 J.-Y., and Diedhiou, A. (2012). An analysis of the diurnal cycle of precipitation over dakar using local
1167 rain-gauge data and a general circulation model. *Quarterly Journal of the Royal Meteorological Society*,
1168 138(669):2182–2195.
- 1169 Sherwood, S. C. and Huber, M. (2010). An adaptability limit to climate change due to heat stress. *Proceedings*
1170 *of the National Academy of Sciences*, 107(21):9552–9555.
- 1171 Stephens, G. L., Wild, M., Stackhouse, P. W. J., L’Ecuyer, T., Kato, S., and Henderson, D. S. (2012). The
1172 global character of the flux of downward longwave radiation. *Journal of Climate*, 25(7):2329–2340.
- 1173 Sultan, B. and Gaetani, M. (2016). Agriculture in west africa in the twenty-first century: climate change and
1174 impacts scenarios, and potential for adaptation. *Frontiers in Plant Science*, 7.
- 1175 Timouk, F., Kergoat, L., Mougou, E., Lloyd, C., Ceschia, E., Cohard, J.-M., De Rosnay, P., Hiernaux, P.,
1176 Demarez, V., and Taylor, C. (2009). Response of surface energy balance to water regime and vegetation
1177 development in a sahelian landscape. *Journal of hydrology*, 375(1):178–189.
- 1178 Voldoire, A., Sanchez-Gomez, E., y Méliá, D. S., Decharme, B., Cassou, C., Sénési, S., Valcke, S., Beau,
1179 I., Alias, A., Chevallier, M., et al. (2013). The cnrm-cm5. 1 global climate model: description and basic
1180 evaluation. *Climate Dynamics*, 40(9-10):2091–2121.
- 1181 Wielicki, B. A., Barkstrom, B. R., Baum, B. A., Charlock, T. P., Green, R. N., Kratz, D. P., Lee, R. B., Minnis,
1182 P., Smith, G. L., Wong, T., et al. (1998). Clouds and the earth’s radiant energy system (ceres): algorithm
1183 overview. *IEEE Transactions on Geoscience and Remote Sensing*, 36(4):1127–1141.
- 1184 Wielicki, B. A., Barkstrom, B. R., Harrison, E. F., Lee III, R. B., Louis Smith, G., and Cooper, J. E. (1996).
1185 Clouds and the earth’s radiant energy system (ceres): An earth observing system experiment. *Bulletin of*
1186 *the American Meteorological Society*, 77(5):853–868.
- 1187 Yasuda, N. (1988). Turbulent diffusivity and diurnal variations in the atmospheric boundary layer. *Boundary-*
1188 *Layer Meteorology*, 43(3):209–221.
- 1189 Zschenderlein, P., Fink, A. H., Pfahl, S., and Wernli, H. (2019). Processes determining heat waves across
1190 different european climates. *Quarterly Journal of the Royal Meteorological Society*.